Quantitative Prediction for Deformation and Brine Extraction in Salt Solution Mining Based on Water-Solution Kinetic (WSK) InSAR Model

Xuemin Xing, *Member*, *IEEE*, *Tengfei Zhang*, *Student Member*, *IEEE*, Jun Zhu, Jiancun Shi, Jiehua Cai, Guanfeng Zheng, and Minchao Lei

Abstract—Long-term deformation prediction and quantitative brine estimation are of great significance for safety precautions and environmental protection in salt mining areas. Traditional Interferometric Synthetic Aperture Radar (InSAR) combined with Probability Integral Method (PIM) has the following limitations: mathematical empirical models are mostly used in InSAR deformation modelling, which ignore the mechanisms of underground mining thus may limit the accuracy of deformation observations; InSAR deformation models have theoretical contradictions and inconsistencies with the future prediction models; PIM is not applicable to the deformation induced by salt solution mining. In this study, a novel Water-Solution Kinetic (WSK) InSAR model was proposed to replace the traditional InSAR models. It considers the principles of substance diffusion and mass transfer of salt, thus can be used directly for the quantitative prediction of both the deformations and extracted brine. Least Squares with Inequality Constraints (LSIC) was introduced to solve the unknown WSK parameters based on the InSAR phases to improve the computational efficiency. Two salt mines in China were selected for the experiments. The results show that the maximum predicted deformation was 296 mm in XR and 155 mm in HR, and the brine composition was estimated to be 0.406 and 1.477 million tons per year, respectively. Compared to traditional Static-PIM, the accuracy was improved by 48.3% and 54.5%, respectively. The results indicated that WSK is more precise and reasonable for predicting the deformation in salt mining areas, which can provide data reference for the management of salt mines.

Index Terms—InSAR, water-solution kinetic, salt mining area, deformation prediction, brine estimation or prediction.

Xuemin Xing, Jun Zhu, Jiancun Shi, Jiehua Cai, Guanfeng Zheng and Minchao Lei are with the School of Traffic and Transportation Engineering for Changsha University of Science and Technology, Changsha 410114, China, and also with the Institute of Radar Remote Sensing Applications for Traffic Surveying and Mapping, Changsha University of Science and Technology, Changsha 410114, China (e-mail: xuemin.xing@csust.edu.cn; jzhu@csust.edu.cn; jc.shi@csust.edu.cn; caijiehua@whu.edu.cn; 212010501-56@stu.csust.edu.cn and lmc@stu.csust.edu.cn).

Tengfei Zhang is with the School of Resource and Environmental Sciences, Wuhan University, Wuhan 430079, China (e-mail: tengfeizhang@whu.edu.cn).

I. INTRODUCTION

CHINA is one of the few countries in the world with extremely rich salt mineral resources, with reserves of about 4.45 trillion tons[1]. Due to the multi-directional exploitation of water-solution, the rock salt caverns are prone to collapse and brine leakage, which may arouse serious damage to the surrounding environment and threat to the safety of human life and property [2]–[4]. Therefore, long-term deformation monitoring and prediction in salt mining areas can ensure the safety of mining activities, provide a reference for mining management and environmental protection [5]–[6].

The Multi-Temporal Interferometric Synthetic Aperture Radar (MT-InSAR) is an advanced earth observation technology developed in recent years, which has proven to have tremendous capabilities for deformation monitoring in mining areas [7]–[14]. However, the single MT-InSAR can only achieve the time series deformation monitoring during SAR acquisitions, which cannot be acquired to predict the displacement beyond the span of the SAR acquisition images. To compensate for this limitation, researchers have combined the Probability Integral Method (PIM) with MT-InSAR technology to predict the forward deformation induced by mining activities [15]–[20]. The basic thought is to use the deformation time series obtained by the InSAR technology as observations for the inversion of the PIM parameters, and then the forward deformations in future periods can be predicted using the PIM prediction model. However, the following limitations still need to be discussed: Firstly, pure mathematical empirical models (i.e., linear, seasonal, and polynomial models) are mostly used in the InSAR deformation modelling process to generate InSAR deformations, which ignore the underground mining mechanisms, thus may limit the accuracy of the deformation observations. In fact, the mining-induced ground deformation shows complex non-linear characteristics temporally. Obviously, a single mathematical empirical model cannot reasonably describe the complex deformation mechanism of underground salt mining process. Secondly, inaccurate InSAR deformation results will transfer unavoidable errors to the estimated PIM parameters, which will then propagate to future predicted results. Thirdly, although the widely used PIM

models are proven to be effective in coal mining areas, it may not be suitable for describing the dynamic processes of water solution extraction in salt mining areas. Finally, combination of Genetic Algorithms (GA) and Least Squares (LS) methods are mostly used for parameter estimation of non-linear InSAR physical models [21]–[22]. Most of these algorithms are based on iterative searching algorithms, which are time consuming and highly dependent on the initial value of the parameters. Consequently, it may lead no solution or large estimation errors induced by non-convergence of the iterations.

In this study, we propose a novel Water-Solution Kinetic (WSK) InSAR prediction model to replace the traditional InSAR models, which considers the principles of substance diffusion and mass transfer. In WSK model, the physical parameters of diffusion coefficient and solution concentration are incorporated into the InSAR deformation model, which can reasonably interpret the temporal non-linear characteristics of the deformations induced by the water-soluble mining activities. In order to estimate the WSK parameters, the Least Squares with Inequality Constraints (LSIC) is introduced here, which can estimate the unknowns based on InSAR phase observations, significantly improve solving efficiency and accuracy. The WSK model and estimated parameters can be used directly to predict the forward deformation and the quantitative brine extraction.

In this work, firstly, the methodology of WSK construction based on the principles of substance diffusion and mass transfer, and the parameter estimation based on LSIC algorithm were introduced respectively. Then, both simulated and real data experiments were designed to verify the novel algorithms. Two salt mines in China, Xinhua Rock Mine (XR) in Hunan Province and Huai'an Rock Mine (HR) in Jiangsu Province, were selected for the real data experiments. Two groups of deformation time series were obtained and the quantitative brine extraction prediction was carried out based on WSK. The accuracy evaluation for WSK modelling, deformation monitoring and prediction were also executed. The spatial-temporal characteristics of the predicted subsidence, especially related to the the substance diffusion and mass transfer law were discussed. A sensitivity analysis for WSK parameters was also showed in the discussions in detail. Finally, the revealed discoveries and the advantages of WSK were concluded.

II. METHODOLOGY

A. Water-Solution Kinetic Subsiding Model

The dissolution process of salts follows the principles of Water-Solution Kinetic, substance diffusion and mass transfer. The relationship between vertical subsidence and the total amount of brine can be written as [23]:

$$Q = Q_0 \times t \times F_0 = S_{sol} \times F_0 \qquad (1)$$

where Q denotes the total amount of extracted brine during the periods between the two interferometric SAR acquisitions; Q_0 is the amount of extracted brine per unit time and area; t is the total time of the mining activity, which can be defined as the temporal periods between the two SAR acquisitions; F_0 is the dissolution area during the water dissolution process; S_{sol} is the vertical subsidence caused by water solution mining, which is treated as the ground subsidence. According to the principle of diffusion and dissolution, Q_0 can be expressed as:

$$Q_0 = D(C_s - C_x)/C_s\delta \qquad (2)$$

where D is the diffusion coefficient, which can be considered as an unknown parameter, the values of D vary on different pixels, but treated as constant temporally; $(C_s - C_x)$ is the solubility of the rock salt, treated as constant spatially across all the pixels in the funnel, but varying temporally, C_s is the concentration index of the saturated solution, which is treated as a constant, C_x is the concentration index of the unsaturated solution, which is treated as an unknown variable; δ is the thickness of the saturated solution layer, which depends on the velocity of the solvent and regarded as a constant here. According to (1) and (2), the time series function of subsidence S_{sol} can be written as:

$$S_{sol}(t) = (D(C_s - C_x)/C_s\delta) \cdot t \qquad (3)$$

where the diffusion coefficient D and solution concentration index C_x are both treated as unknown WSK parameters. Function (3) describes the temporal relationship between subsidence and WSK parameters, which can assist in interpreting the temporal non-linear characteristics of the water-soluble extraction induced deformations.

B. Time series InSAR Modelling Based on WSK

Suppose that $N+1$ SAR images are acquired, and M interferometric pairs are generated. For each pixel of high coherence in i-th interferogram [24]–[26], the interferometric phase can be expressed as:

$$\delta\varphi_m^i = \delta\varphi_{def}^i + \delta\varphi_{topo}^i + \delta\varphi_{orbit}^i + \delta\varphi_{atm}^i + \delta\varphi_{noise}^i + \delta\varphi_{non}^i$$
$$\approx \frac{4\pi}{\lambda}\Delta d^i + \frac{4\pi B_i}{\lambda R \sin\theta}\Delta H^i + \Delta\varphi_{res}^i \qquad (4)$$

where λ represents the radar wavelength; Δd^i represents the deformation along the line-of-sight (LOS) direction at the i-th high-coherence point of the m-th differential interferogram, referred as the Low-Pass (LP) deformation component; $\delta\varphi_{topo}^i$ represents the topographic phase, $\delta\varphi_{topo}^i = \frac{4\pi B_i}{\lambda R \sin\theta}\Delta H^i$, where θ and B_i represents the radar incident angle and the perpendicular baseline, respectively; R is the sensor-target distance; ΔH^i is the elevation correction, which is unknown for the i-th pixel and considered temporally constant; $\delta\varphi_{def}^i$ represents the deformation phase; $\delta\varphi_{orbit}^i$ represents the orbital error; $\Delta\varphi_{res}^i$ represents the residual phase, which mainly includes the atmospheric delay phase $\delta\varphi_{atm}^i$, the noise phase

$\delta\varphi_{noise}^i$ and the High-Pass (HP) deformation composition $\delta\varphi_{non}^i$ [27]. When the horizontal movement of the ground surface is ignored, the relationship between LOS deformation and vertical subsidence can be written as:

$$\Delta d^i = d_{LOS}(t_B) - d_{LOS}(t_A) = \left[S_{sol}(t_B) - S_{sol}(t_A) \right] \cdot \cos\theta \quad (5)$$

where $d_{LOS}(t_B)$ and $d_{LOS}(t_A)$ are the deformations at dates t_B and t_A respectively with the reference time $t_0 = 0$; similarly, $S_{sol}(t_B)$ and $S_{sol}(t_A)$ are water-solution related subsidence respectively at t_B and t_A with respect to the time $t_0 = 0$, where $d_{LOS}(t_0) \equiv 0$ and $S_{sol}(t_0) \equiv 0$. Substituting (5) into (4), the function between InSAR phases and WSK parameters can be expressed as:

$$\delta\varphi_m^i = \frac{4\pi}{\lambda} \left[D(C_s - C_x) \Delta t / C_s \delta \right] \cdot \cos\theta + \frac{4\pi B_i}{\lambda R \sin\theta} \Delta H^i + \Delta\varphi_{res}^i \quad (6)$$

suppose $GP = [C_s, \delta]$ defines the geological parameters, which are considered as the known parameters and can be determined according to the geological conditions in the mining area. Both the WSK parameters $WP = [D, C_x]$ and ΔH^i are treated as unknown parameters, written as $X^T = [D, C_x, \Delta H^i]$, and can be estimated by LSIC as introduced in Section II-C. Substituting X into function (3), the time series deformations both within and beyond the SAR acquisitions can be generated.

C. WSK Parameters Estimation Based on LSIC Algorithm

GA has been widely used to solve the problem of estimating non-linear parameters in InSAR physical model. However, its disadvantage is time consuming and low accuracy [22]. Since (6) can be transformed into a linear least square parameter estimation problem, we propose here the LSIC algorithm for solving (6) [28]–[29]. The algorithm is based on the least square estimation, which can avoid the time-consuming searching process of GA, accordingly improve the velocity of convergence. The uniqueness and stability of the parameters can be ensured by additional inequality constraints, which make LSIC more accurate than GA searching. The functional model for LSIC can be expressed as:

$$\begin{cases} \text{Model: } \varphi = AX + v \\ \text{Constraint: } CX \leq W \end{cases} \quad (7)$$

where φ represents the interferometric phase observations in (6). A is the coefficient matrix; X represents the unknown parameters; v represents the random error vector; C is the coefficient matrix of the unknown vectors; and W is the constant vector. Therefore, the fitness function here can be written as:

$$\begin{cases} f_{min} = (AX - \varphi)^T P(AX - \varphi) \\ \text{Constraint: } CX \leq W \end{cases} \quad (8)$$

where P is the weight matrix, considered as the identical matrix here; According to the previous consulting and investigation, the following inequality constraints can be constructed:

$$\begin{cases} 0 \leq D \leq W_1 \\ 0 \leq C_x \leq W_2 \\ \left| \Delta H^i \right| \leq W_3 \end{cases} \quad (9)$$

where W_1, W_2 and W_3 are the corresponding boundary values for D, C_x and ΔH^i, respectively. Among them, D is within the range of [0, 1.87] $\times 10^{-9}$ m²/s, C_x within [0, 48.8] g/100gH₂O, and ΔH^i within [-20, 20]m [30]–[32]. Based on (8) and (9), the optimized unknown parameters can be generated iteratively.

D. Quantitative Brine Composition Prediction

According to the principle of Water-Solution Kinetic, the brine composition can be expressed as [23]:

$$T_y = FHGE = \frac{1}{4}\pi HGEd^2 + L_s HGEd \quad (10)$$

where T_y is the brine composition of the salt mining area; H is the thickness of the mining layer; G and E are the weight and the average grade of the ore, respectively, which can be considered as known parameters; F is the total dissolution area during the development of the dissolution cavity; d is the diameter of the dissolution channel, which is treated as an unknown parameter here. As shown in Fig. 1(a) and (b), the shape of the dissolution cavity is approximately regarded as a long slot with a rectangular column in the middle and semi-cylindrical ends. The diagrammatic sketch of cavern and surface subsidence induced by salt mining activities is shown in Fig. 1(b) and (c).
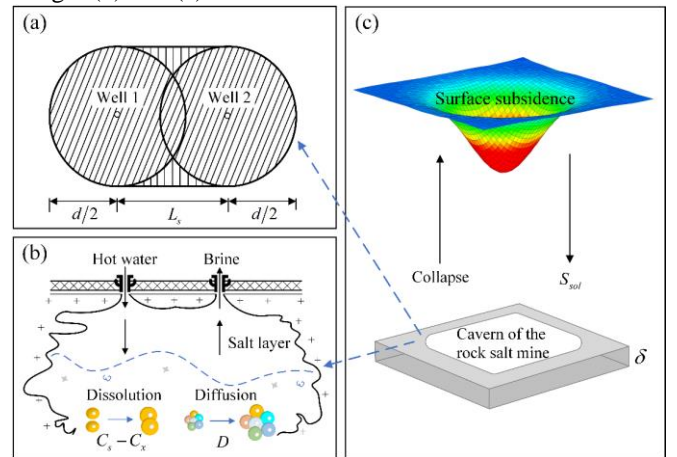

Fig. 1. Diagrammatic sketch of cavern and surface subsidence induced by salt mining activities. (a) Top view of the dissolution cavities. (b) Side profile of the dissolution and diffusion processes of salts in the cavern. (c) 3D view of the surface subsidence.

When ignoring the horizontal movement, the total dissolution area can be expressed as $F = \pi d^2/4 + L_s d$ (where L_s is the distance between the well groups, which is

determined in the design materials of the mining companies). The brine composition for the area can be expressed as:

$$T_y = Q \cdot g \tag{11}$$

where g represents the average content of the primary brine composition. Substituting (11) into (10), it can be derived:

$$d = \frac{-L_s + \sqrt{L_s^2 + \dfrac{\pi Q g}{HGE}}}{0.5\pi} \tag{12}$$

where L_s, H, G, E, and g can be determined by investigating the geological structure of the study area [33]–[35]. According to (1), the total amount of brine Q at time t can be written as:

$$Q = \sum_{i=1}^{k} S_{sol}(t) \times F_0 \tag{13}$$

where k is the total number of pixels covering the image, $S_{sol}(t)$ is corresponding vertical subsidence of the i-th high coherence point, which can be predicted following (3). Substituting (13) into (12), the diameter d can be estimated, and then the corresponding quantitative brine composition T_y at time t can be predicted following (10).
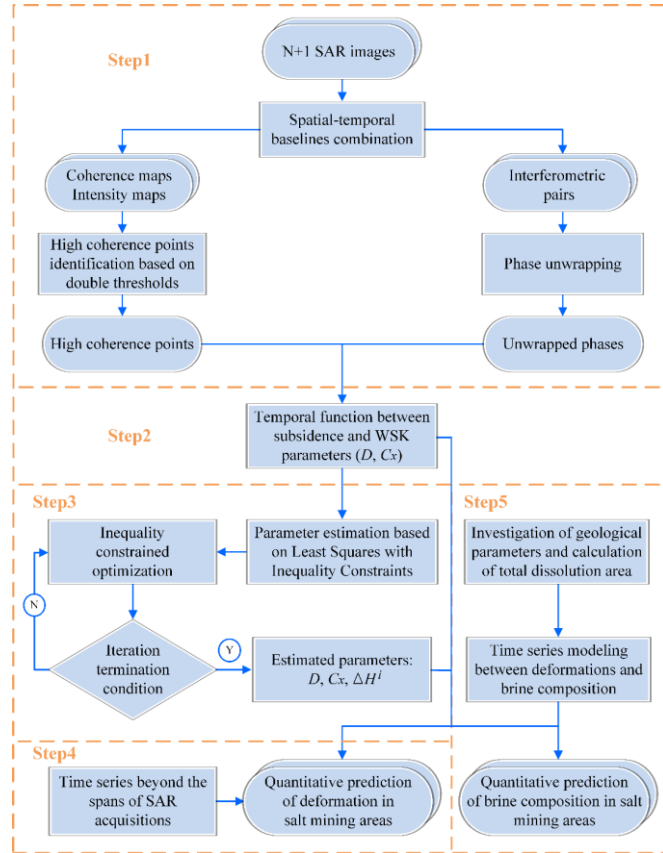
E. Flow chart and Process Steps

Fig. 2. Flow chart of quantitative prediction for both deformations and brine extraction based on WSK.

Fig. 2 shows the process flow of quantitative prediction for both time series deformations and quantitative brine extraction based on the WSK model. The specific steps are as follows: (1)

Differential interferometric processing and identification of high-coherence points based on the double-threshold methods; (2) Time series InSAR modelling based on WSK; (3) WSK parameters estimation based on InSAR phases by the LSIC algorithm; (4) Forward dynamic subsidence prediction after the spans of SAR acquisitions; (5) Time series modelling between the subsidence and the extracted brine composition, and quantitative prediction for brine composition.

III. EXPERIMENTS AND RESULTS

A. Simulated Experiment

A simulated experiment was designed in order to verify the feasibility and reliability of the proposed method. The space parameters of the Sentinel-1 A SAR images have been used for the simulation of the satellite parameters. The geological parameters were set as $GP = [40.8\text{g}/100\text{gH}_2\text{O}, 3\text{ m}]$. The initial intervals for the magnitude of the unknown parameters were introduced in Section II-C, and the parameters D, C_x and ΔH^i were simulated by 2-D Gaussian function, seasonal function and Gaussian random simulator, respectively. The real subsidence field can be generated according to (3), which can be used to evaluate the accuracy of the estimated subsidence. Totally, 500 pixels are extracted from the field for quantitative comparison. The interferometric phases were simulated according to (6). Random noise levels within 0~0.65 rad were added respectively, the random noise can be expressed as $Noi = sqrt(0.65) * rand(60,60)$, where Noi represents the noise; $sqrt(0.65)$ represents the variance of 0.65rad; $rand(60,60)$ is total simulated size of the phase function by random noise function [32] – [33]. The WSK parameters can be estimated by LSIC, which can be used to generate the predicted time series subsidence field. In order to quantitatively evaluate the accuracy of the WSK parameters, the relative error for each parameter was calculated under the noise levels of 0.05 rad, 0.25 rad, 0.45 rad and 0.65 rad, respectively (as shown in Table I). The smaller the relative errors are, the higher is the accuracy of the estimates of the parameters. From the Table I, the errors of the parameter gradually increase with the noise level. Even with a high noise level of 0.65rad, the relative errors of the three unknown parameters are lower than 6.0% (the highest relative error is 5.8% for D), which indicates the feasibility and reliability of LSIC algorithm.

TABLE I
RELATIVE ERRORS OF PARAMETERS UNDER DIFFERENT NOISE LEVELS

Parameters	Noise level			
	0.05 rad	0.25 rad	0.45 rad	0.65 rad
D	0.4%	2.2%	4.1%	5.8%
C_x	0.3%	2.0%	3.6%	4.2%
ΔH^i	0.2%	1.6%	2.7%	3.2%

Fig.3 shows the comparison between the predicted deformation by WSK parameters and the simulated real deformation at the 500 extracted pixels with a high noise level

of 0.65 rad. Obviously, the predicted deformation results maintain good consistency with the real subsidence even with a high noise level of 0.65 rad. According to the quantitative statistics of Fig. 3(a) to 3(h), the number of points with the deviations within [-3, 3] mm accounts for 100%, 100%, 93.4%, 84%, 78.6%, 75.4%, 72%, and 71%, respectively, and the maximum deviations are 0.4 mm, 2.9 mm, 5.9 mm, 8.4 mm,

9.8 mm, 11.8 mm, 13.1 mm, and 14.2 mm, respectively. The red broken line in Fig. 3(h) represents the deviations of all the pixels at 792 days, with the maximum deviation as 14.2 mm, which only accounts for 6.3% of the maximum deformation 225 mm. The RMSE between the predicted and the real subsidence was estimated as ±5.4 mm, which proves the theoretical feasibility of the WSK model.
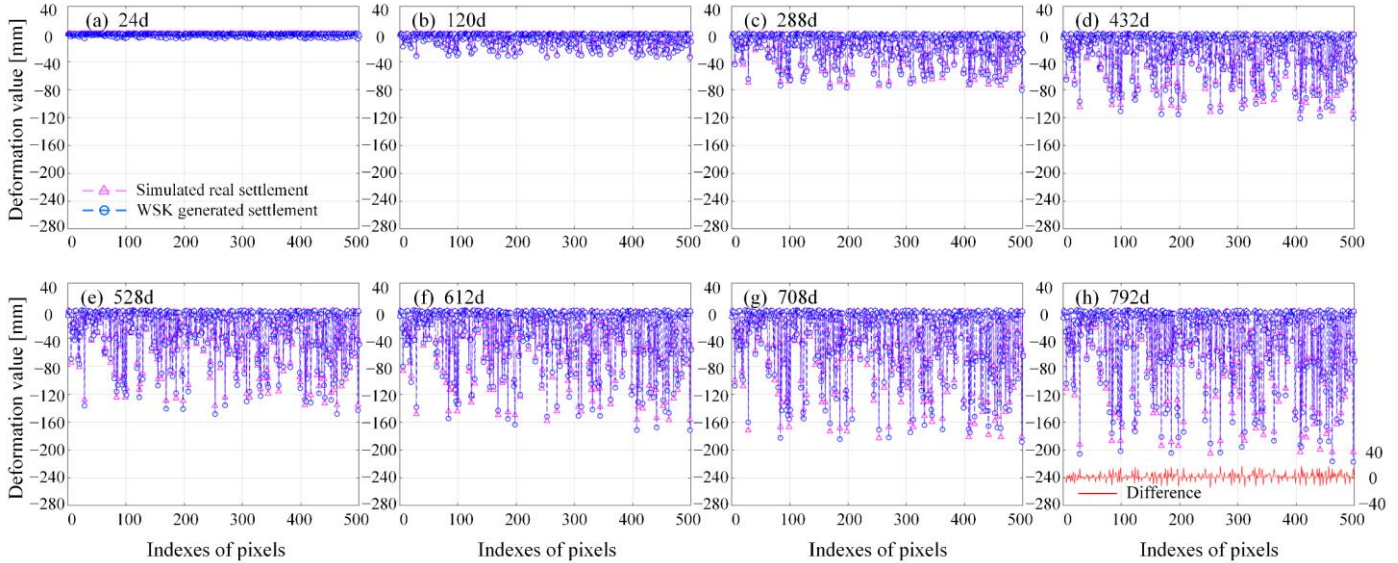

Fig. 3. Comparison between the predicted subsidence and the simulated real settlement. (a) 24 days. (b) 120 days. (c) 288 days. (d) 432 days. (e) 528 days. (f) 612 days. (g) 708 days. (h) 792 days.

B. Real Data Experiment

1) Study Area and SAR Data Preprocessing: Two typical salt mines, XR in Hunan Province and HR in Jiangsu Province, China, were selected as the study areas (as shown in Fig. 4). The red rectangles in Fig. 4(a) represent the spatial coverage of the Sentinel-1A (ascending) data covering the two study areas, and the purple rectangles are the two interested salt mines. Both the XR and HR areas are extremely rich in salt resources, not only in terms of reserves, but also with high salt content and relatively concentrated distribution [34]–[35].

The XR located in the Liyang Plain, the inclination angle is 3~5°, the burial depth is 200~300 m, and the thickness of the mining layer is 3 m [33]. The HR area located in the Huaian Salt Basin and Hongze Salt Basin, with an inclination angle of 5°~9°, a burial depth of 600~800 m, and a mining layer thickness of 5 m [34]. The continuous exploitation of mineral resources has caused accumulated changes in the structure of underground rock formations, which induces potential damage to the surrounding environment and infrastructures. According to our in-situ investigation, brine pumping and water salinization have caused ground cracks and brine leakage salinization in some areas (as shown in Fig. 5).
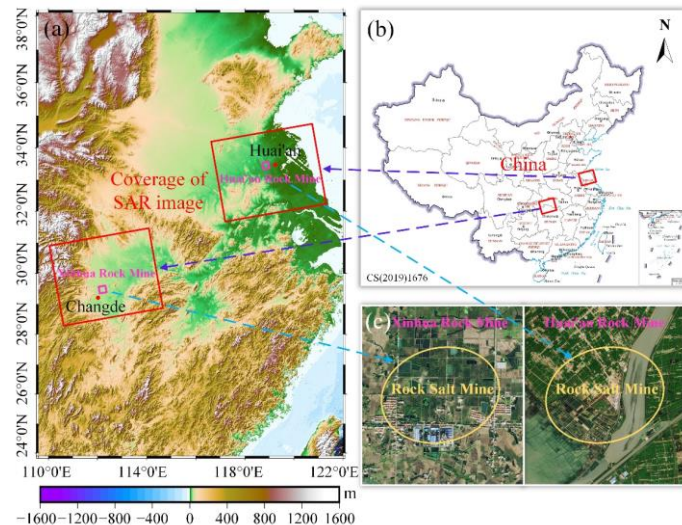

Fig. 4. Map of the study area. (a) Coverage of SAR images. (b) Map of China. (c) Satellite images of the study area.
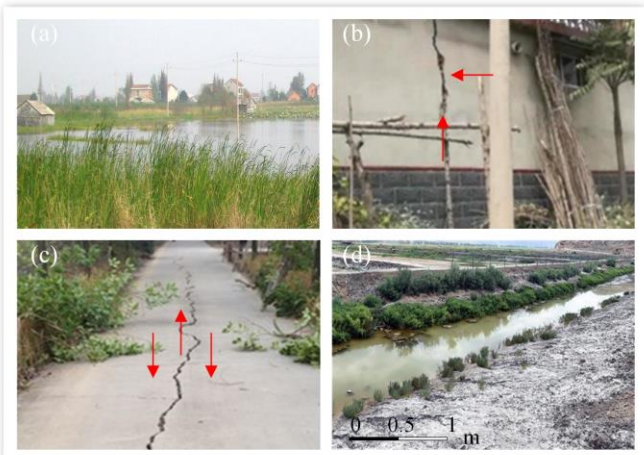

Fig. 5. Geological and environmental damages in salt mining areas. (a) Brine leakage. (b) Crack on the wall. (c) Crack on the ground of road. (d) Salinization.

A total of 32 and 35 scenes of Sentinel-1A SAR images covering the XR area from June 15, 2015 to March 28, 2017 and the HR area from March 28, 2017 to March 28, 2019, respectively, were collected. The coherence maps, intensity maps and unwrapped interferometric pairs with small spatial-temporal baselines were generated via GAMMA, and the high coherence point identification, time series InSAR deformation modelling, WSK parameter estimation, time series deformation prediction and quantitative brine prediction were all implemented via Matlab software. The terrain phase was filtered using the Shuttle Radar Topography Mission Digital Elevation Model (SRTM DEM) data provided by NASA with a resolution of 30 m [36], and the orbital error was removed by polynomial fitting model. Minimum Cost Flow (MCF) was used to carry out the phase unwrapping processing [37], and the atmospheric phase delay was suppressed by Gacos (http://ceg-research.ncl.ac.uk/v2/gacos/) [38].

2) WSK parameter estimation by LSIC: According to the in-situ investigation, the geological parameters were set as $GP = $ [48.8 g/100gH$_2$O, 3 m] in XR and $GP = $ [48.8 g/100gH$_2$O, 5 m] in HR, respectively. The first 24 images of the XR (from June 15, 2015 to January 11, 2017) and 29 images of the HR

(from March 28, 2017 to March 6, 2019) were used to estimate the WSK parameters $WP = [D, C_x]$, following Step (3) introduced in Section II-E. The WSK parameters estimated by the LSIC algorithm in XR are shown in Fig. 6, where the values of D are shown in Fig. 6(a), and the values of ($C_s - C_x$) in (6) are shown in Fig. 6(b). D is within [0.78219720, 0.78219880], it can be found interestingly that the values D for the pixels in XR contain several red funnels but are not separately distributed. Each funnel is with dark red in the center and progressively lighter from the center outwards. The funnels are interconnected. This phenomenon is consistent with the spatial distribution characteristic of the deformations which will be discussed in Section V. The solubility ($C_s - C_x$) of the funnel at different temporal points are shown as Fig.6 (b), which shows similar seasonal variations with time series variations of the deformations. According to our estimated results of those two parameters, both the values of D and ($C_s - C_x$) are minor, but the corresponding deformation is high. This phenomenon will be discussed in the sensitivity analysis part in Section V-B.
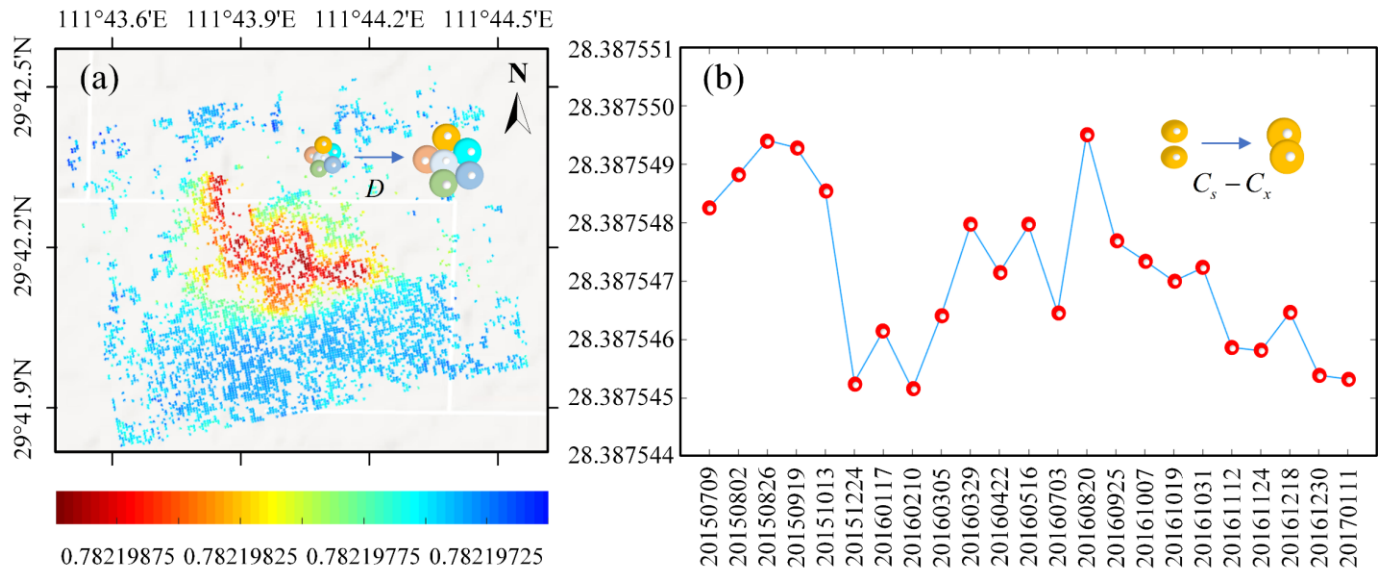

Fig. 6. Estimated WSK parameters. (a) Estimated D for XR. (b) Estimated ($C_s - C_x$) for XR.

3) Deformation Prediction Based on WSK: Fig. 7 shows the estimated and predicted deformations respectively. The last 8 images of the XR (from February 16, 2017 to August 15, 2017) and 6 images of the HR (March 30, 2019 to July 28, 2019) were used for deformation prediction following Step (5) in Section II-E, respectively. Spatially, we can see that the boundary of the settlement funnel can be clearly defined, with a deeper center and a shallower periphery. The center of the funnel started subsiding on July 3, 2016 and gradually spread outwards, changing from light green to dark yellow. Until January 11, 2017, a clear red funnel with stratification formed. From August 15, 2017, the central area became dark red and the settlement funnel was interconnected. Temporally, from July 9, 2015 to February 10, 2016, an overall slow subsidence

trend played a major role, with color varying from blue to light green, and the maximum subsidence of 59 mm. From March 5, 2016 to January 11, 2017, with the further progress of mining, the study area obviously gradually intensified from light green to dark red. On January 11, 2017, the maximum subsidence was 209 mm. The maximum predicted subsidence was up to 298 mm on July 28, 2019.

Similarly, for HR, as shown in Fig. 8, the boundary between the settlement funnel and the outside of the mine is more pronounced. Dissimilarly, a spatial integral subsiding dominated HR area and no obvious funnel can be extracted. In the time series, the maximum accumulated settlement was 123 mm at March 6, 2019 and the maximum predicted subsidence was up to 156 mm.

> REPLACE THIS LINE WITH YOUR MANUSCRIPT ID NUMBER (DOUBLE-CLICK HERE TO EDIT) <
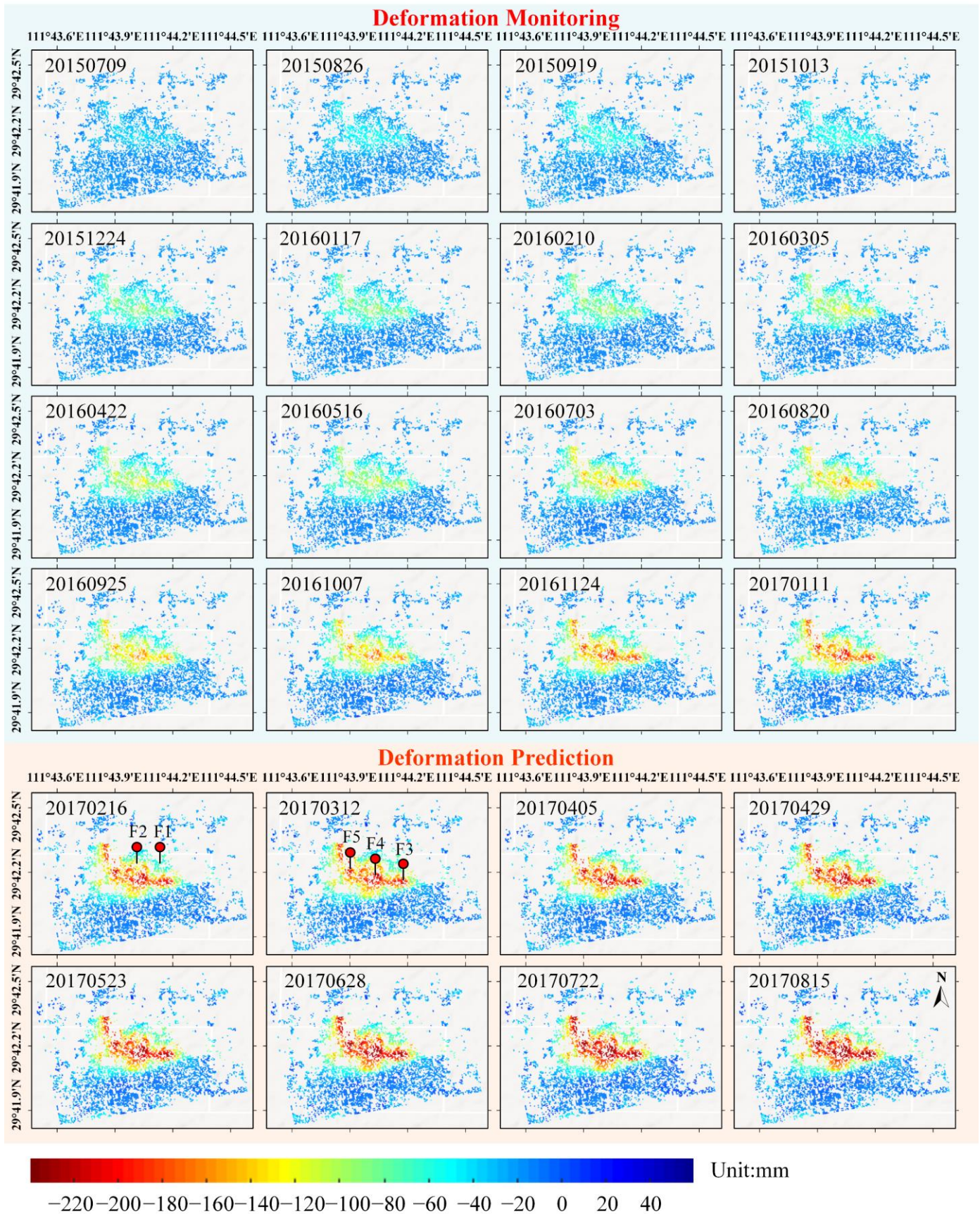

Fig. 7. Time series monitored and predicted deformations of XR (reference date: June 15, 2015).

> REPLACE THIS LINE WITH YOUR MANUSCRIPT ID NUMBER (DOUBLE-CLICK HERE TO EDIT) <
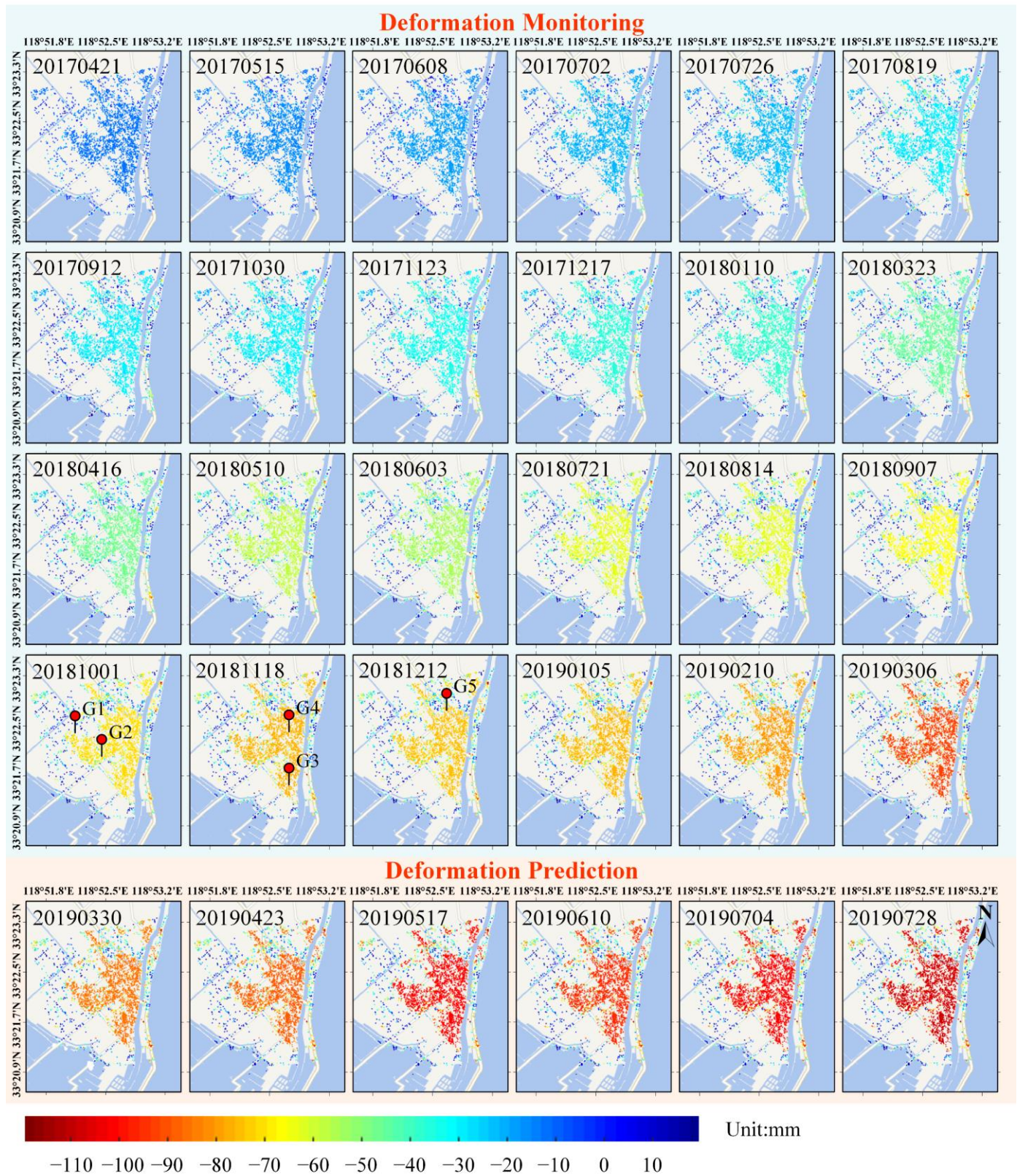

Fig. 8. Time series monitored and predicted deformations of HR (reference date: March 28, 2017).

4) Quantitative Brine Extraction Prediction Based on WSK: As introduced in Section II-D, the quantitative extracted brine can be estimated following Step 5 based on the time series deformation. The parameters L_s, G, E, and g were set as 56.4 m, 2.15 t/m³, 0.52 t/m³, and 80%, respectively, and H were set as 3 m in XR and 5 m in HR, respectively [22]. The dissolution area F_0 was set as 66.47 m², which follows both the multi-look ratio and spatial resolution of Sentinel-1A satellite image. In simple terms, ideally about 15045 (i. e. 1000 m/9.022 m×1000 m/7.368 m≈15045) pixels along the LOS direction can generate an area of 1 km² with a multi-look ratio of 5:1. F is the accumulated area of F_0 over all the subsiding pixels [15].

According to the in-situ geological investigation of the two areas, the method of two-well or multi-well connection extraction had been adopted for water-soluble extraction. According to our results, single settlement funnel was identified around each well. As introduced in Section II-D, the primary brine composition can be estimated according to the cavity diameters d, in order to explore the disciplines of the cavity diameters variations for each settlement funnel, the two areas were divided into six sub-funnels around each water-soluble sub-well (as shown in Fig. 9). The estimated values of the cavity diameters and the quantitative brine compositions for XR (from June 15, 2015 to August 15, 2017) and HR (from March 28, 2017 to July 28, 2019) are shown in Fig. 10 and Fig. 11, respectively.

It can be indicated from Fig. 10 and Fig. 11 that with the processing of water-soluble extraction, areas of the dissolution cavity funnel became larger, and more brine composition were extracted. The estimated values of the cavity diameters gradually increased with the continuous mining active exploitation of brine. The final predicted brine compositions were approximately 0.406 for XR and 1.477 million tons per year for HR, respectively. By consulting historical materials of the mining companies, the predicted results by our method shows good consistency with the actual brine compositions recorded in the mining companies, which indicates that the proposed InSAR WSK model can provide a practical and reliable Remote Sensing method for quantitative brine quantity extraction estimation.
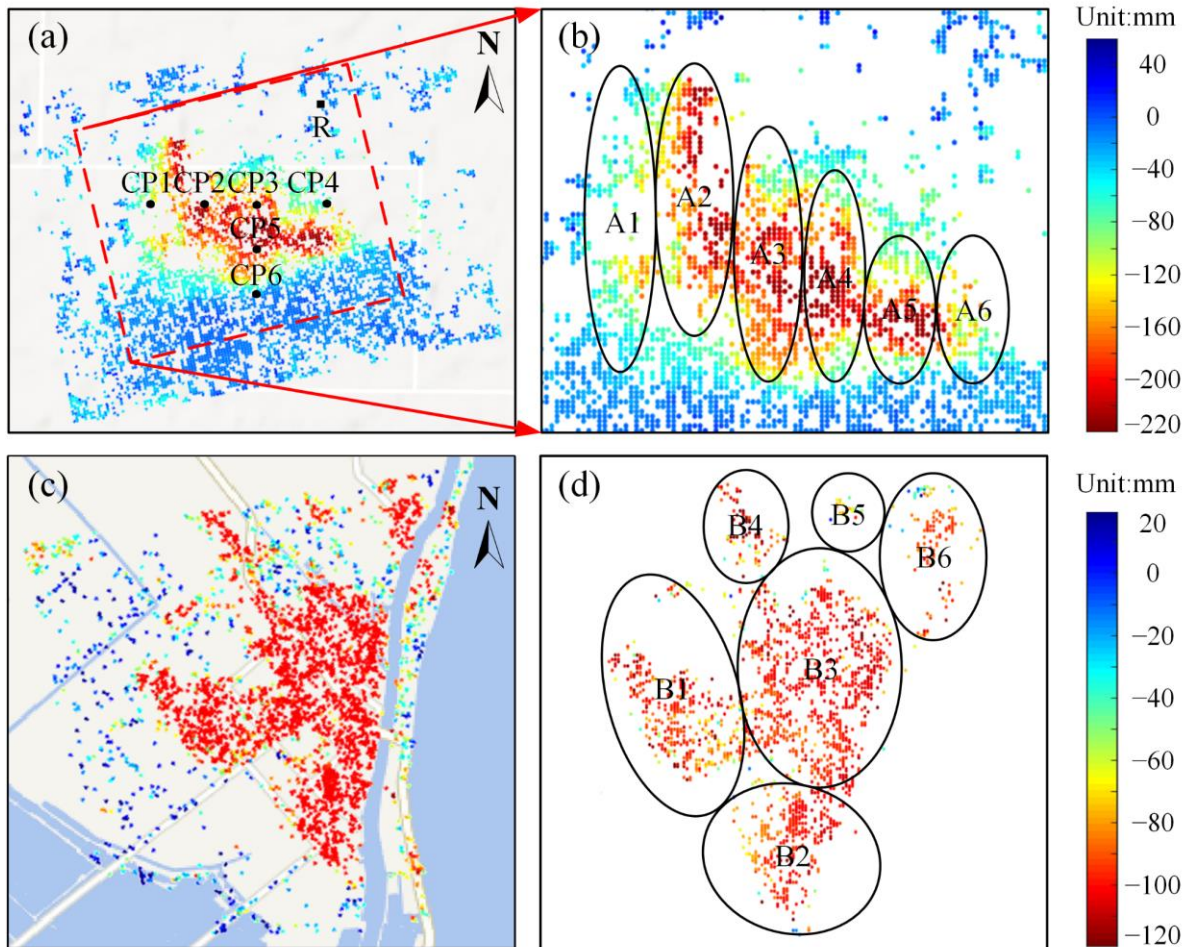

Fig. 9. Schematic of the distribution of sub-settlement funnels. (a) Settlement results obtained by WSK in XR on August 15, 2017. (b) Distribution of sub-settlement funnels in XR. (c) Settlement results obtained by WSK in HR on July 14, 2017. (b) Distribution of sub-settlement funnels in HR.
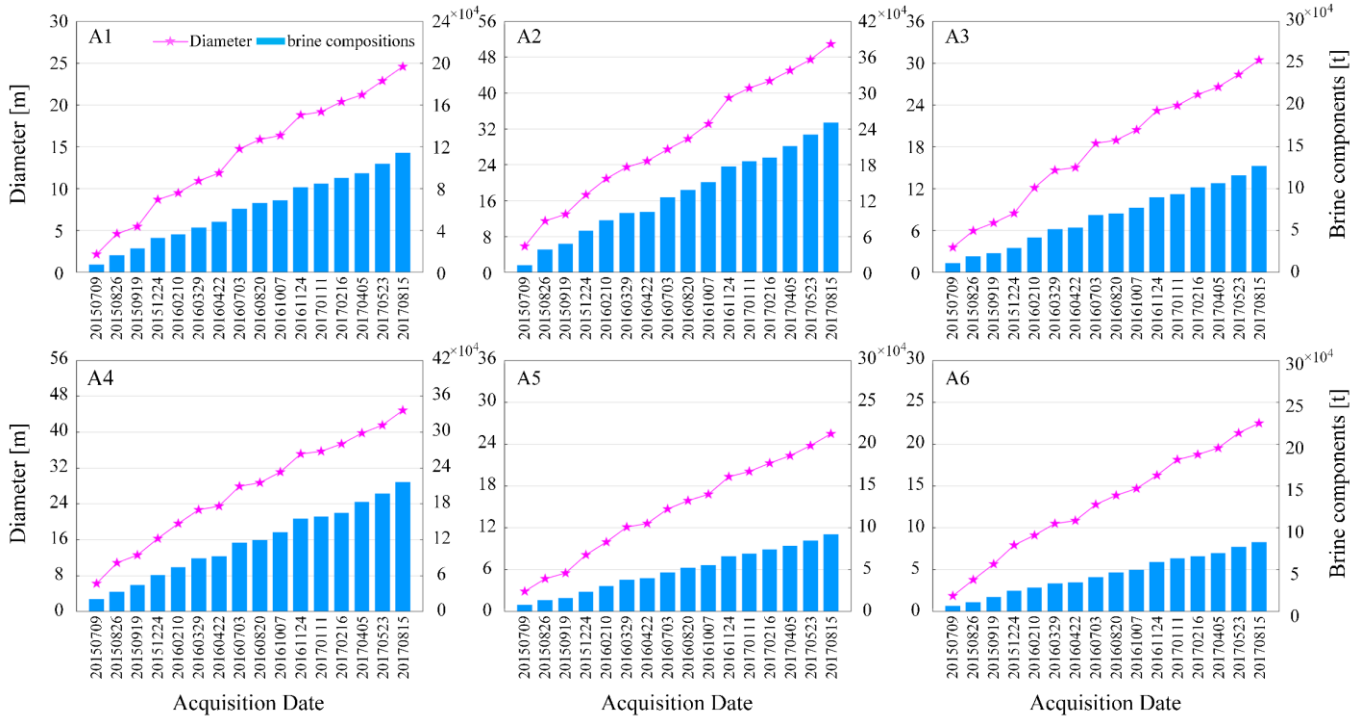
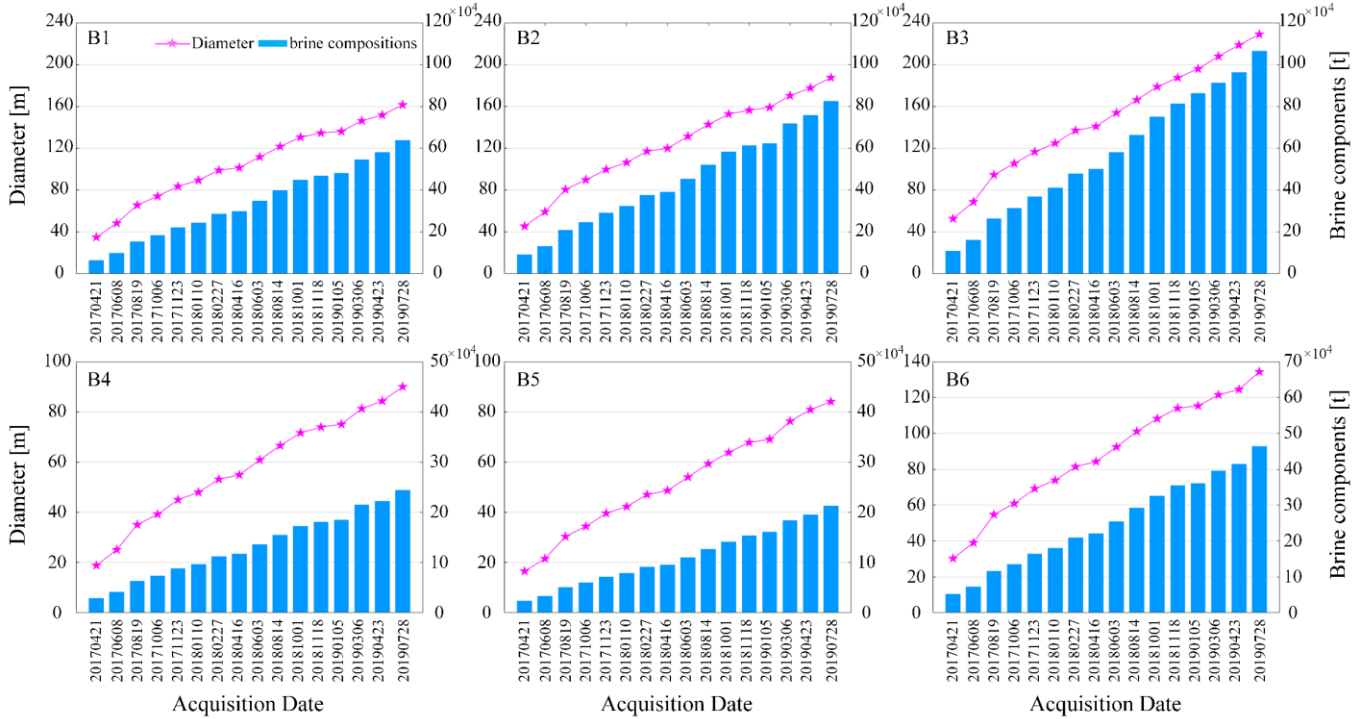**Fig. 10.** Brine compositions for six settlement funnels in XR.

Fig. 11. Brine compositions for six settlement funnels in HR.

IV. ACCURACY EVALUATION

A. Accuracy Evaluation for WSK Deformation Modelling

According to the literature [39], the residual phase can be used to verify deformation modelling accuracy in InSAR time series deformation modelling. Empirically, a lower residual phase in the interferometric pairs indicates a higher modelling accuracy. The average residual phases of each interferogram

obtained by WSK are compared with that of traditional SBAS-InSAR, shown as Fig. 12. Obviously, we can see that the overall amplitude of WSK-generated residual phases is lower than that of SBAS-InSAR, indicating that WSK is more suitable for water-soluble mining-induced ground subsidence. For XR, the Standard Deviation (STD) of the residual phases obtained by WSK was estimated as ± 0.32 rad, with an improvement of 45.7% compared to SBAS-InSAR. Similarly,

for HR, the STD of the residual phases was ± 0.34 rad, with an improvement of 48.8%.
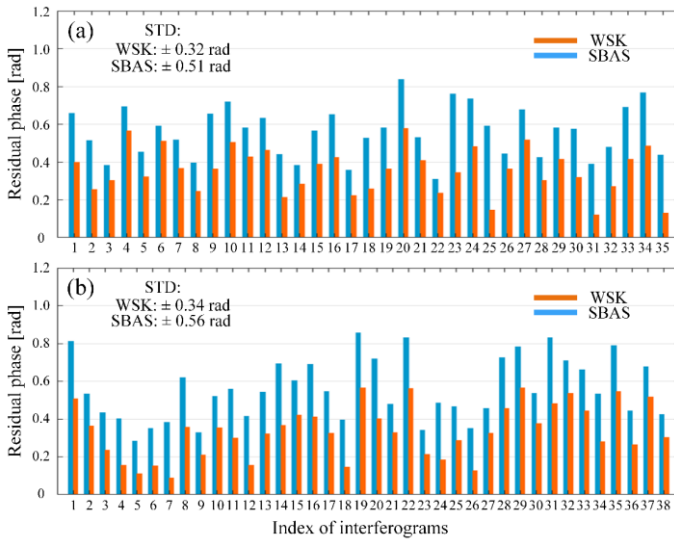

Fig. 12. Residual phase comparison. (a) The XR area. (b) The HR area.

In addition, another accuracy index, namely Akaike's Information Criterion (AIC) index from information theory, is introduced here to evaluate the modelling accuracy. The AIC index can be estimated following the equation of $AIC = Ni\ln(RSS/Ni) + 2(Ku+1)$. Here Ni represents the number of high coherence points; RSS represents the sum of squares of the residual phases; Ku is the number of unknown parameters of the model). Based on the estimated AIC index value, the accuracy of the model can be calculated following:

$PAIC = e^{-0.5\Delta AIC}/1 + e^{-0.5\Delta AIC}$, where ΔAIC is the difference between the AIC indices of the two different comparative models. The more accurate models are those with a lower AIC. Here the estimated AIC index of WSK was 5.74, and 8.34 for that of SBAS-InSAR, with an improvement of 18.3%. Comparatively, for HR, the AIC index of WSK was estimated as 1.15 compared to 2.89 of SBAS, with a 29.5% improvement. The comparative results show another potent proof for the better modelling accuracy of WSK.

B. Accuracy Evaluation for WSK Deformation Monitoring

In order to verify the external accuracy of the monitored deformation in salt mining areas, the historical levelling measurement data from August 2, 2015 to December 18, 2016 were collected in XR. The locations of the levelling points (CP1, CP2, …, CP6) are shown in Fig. 9(a), with the reference point marked as R in the northeast corner. Fig. 13 shows the comparison of WSK-generated deformation time series and the levelling measurements, compared with that of SBAS-generated deformations. The RMSE of the WSK results was estimated as ±5.4 mm, whereas that of SBAS-InSAR was ±8.5 mm, with an improvement of 44.6%. The most serious subsidence point was located at CP3 with the maximum subsidence of 138 mm, the RMSE of WSK only accounts for 3.9% of the maximum deformation, which indicates the promising accuracy of WSK for time series deformation monitoring for ground subsidence induced by water-soluble mining activities.
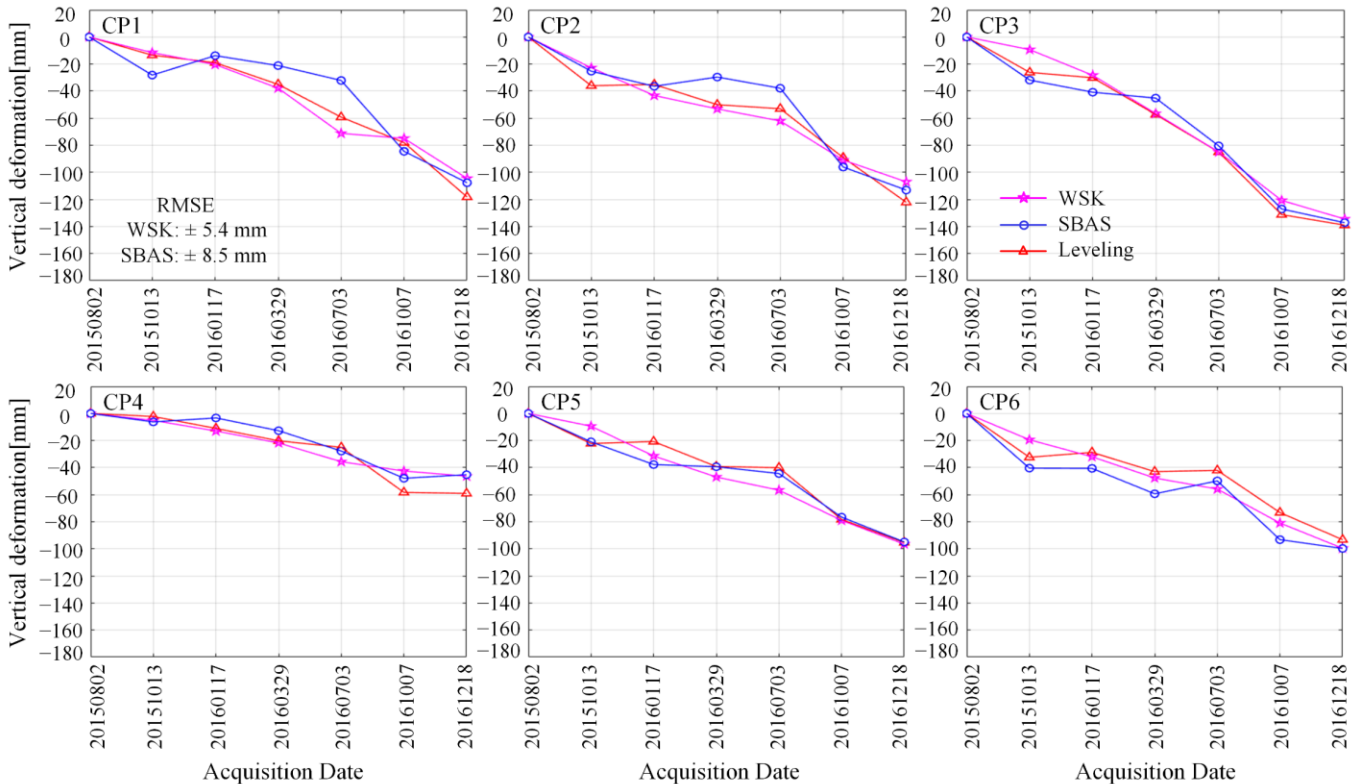

Fig. 13. Comparison with levelling measurements in XR (reference date: August 2, 2015).

C. Accuracy Evaluation for WSK Deformation Prediction

As described in Section III-B, the remaining 8 images of the XR (from February 16, 2017 to August 15, 2017) and the 6 images of the HR (from March 30, 2019 to July 28, 2019) were retained to predict the deformation after the span of the SAR acquisition images. To compensate for the unavailability of simultaneous levelling periods, the SBAS-derived results were used for comparison with the WSK prediction results. The comparison with the WSK prediction results was carried out using the traditional Static-PIM and the Coordinate Time function (CT-PIM) as introduced in [20], [33], [40]. Four periods of deformation prediction for XR (from June 15, 2015 to May 16, 2017, April 5, 2017, June 28, 2017, and August 15, 2017, respectively) and HR (from March 28, 2017 to March 30, 2019, May 17, 2019, June 10, 2019, and July 2019, respectively) were extracted for the quantitative comparative analysis. The deviations and probability distributions between the deformation predictions generated by WSK, CT-PIM and Static-PIM were shown as Fig. 14 and Fig. 15, respectively.
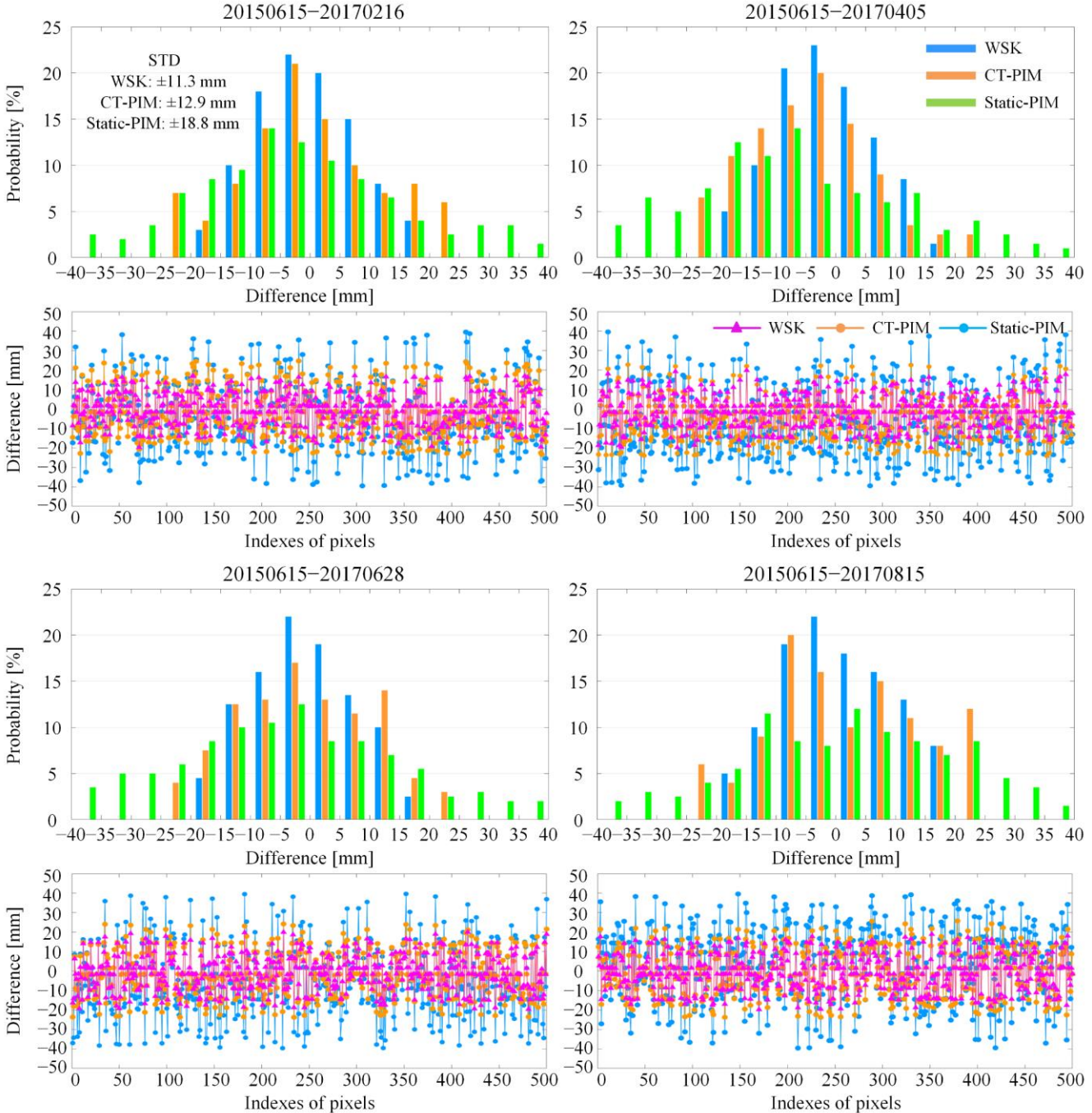

Fig. 14. Deformation deviations between different deformation prediction models and SBAS-InSAR in XR (reference date: June 15, 2015).

It can be seen from Fig. 14 and Fig. 15 that the WSK has better consistency with the SBAS-InSAR monitored time series. In order to show the quantitative accuracy comparisons, three accuracy indicators: STD, Maximum error and Error range were estimated, which are shown as Table II and Table III, respectively. Obviously, both the three indicators for WSK

are lower than those for CT-PIM and Static-PIM. The total STD of WSK was estimated as ±11.3 mm, with an improvement of 48.3% compared to that of Static-PIM; ±7.2 mm for HR, with an improvement of 54.5%. This further proves that the WSK has better accuracy in predicting the deformation of salt mining areas.

TABLE II
ACCURACY INDICATORS FOR WSK DEFORMATION PREDICTION IN XR.

Accuracy indicators	WSK	CT-PIM	Static-PIM
STD (mm)	±11.3	±12.9	±18.8
Maximum error (mm)	19.2	24.6	39.2
Error range (mm)	[−20, 20]	[−25, 25]	[−40, 40]

TABLE III
ACCURACY INDICATORS FOR WSK DEFORMATION PREDICTION IN HR

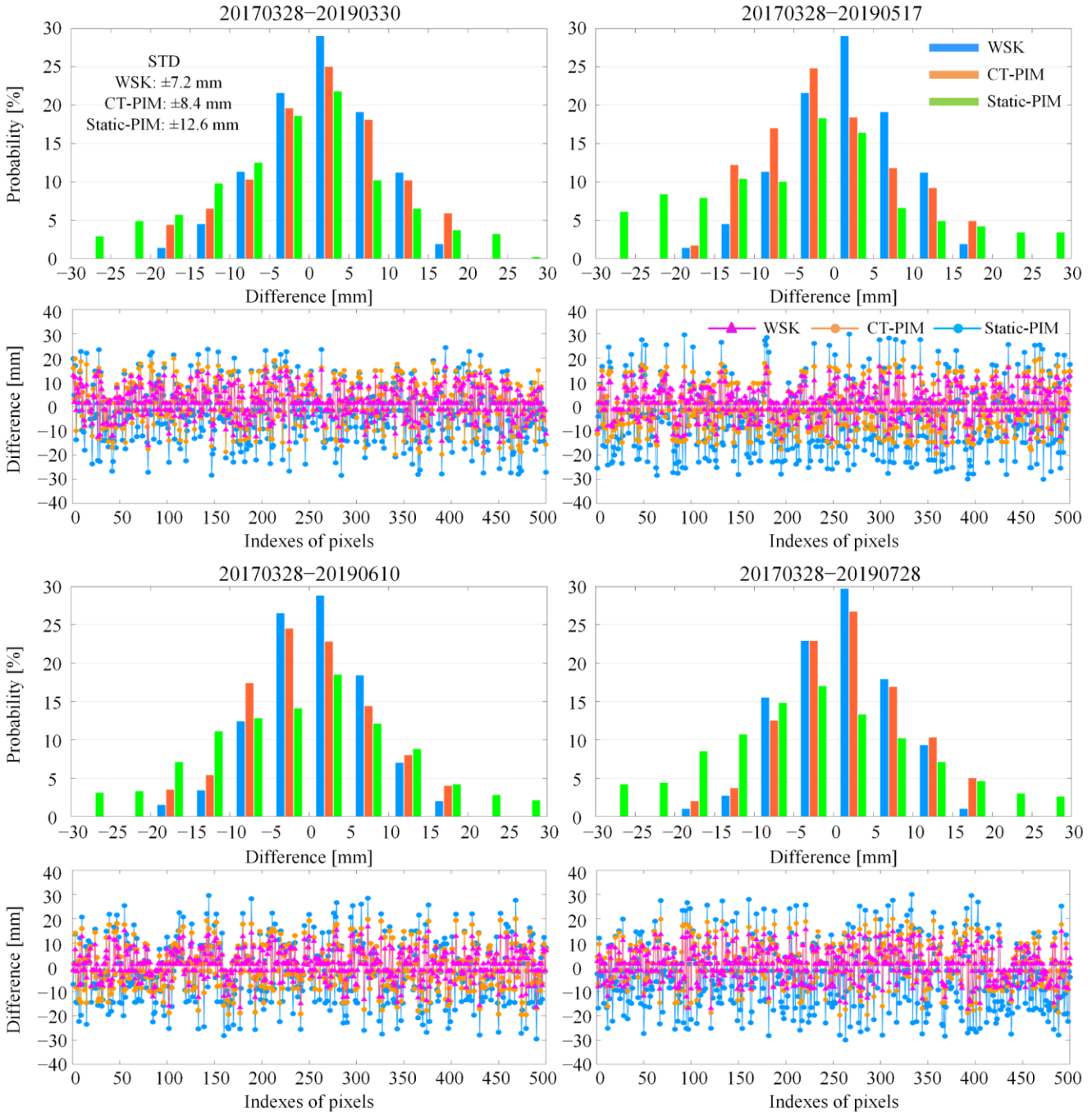| Accuracy indicators	WSK	CT-PIM	Static-PIM
STD (mm)	±7.2	±8.4	±12.6
Maximum error (mm)	17.2	19.6	28.6
Error range (mm)	[−20, 20]	[−20, 20]	[−30, 30]

Fig. 15. Deformation deviations between different deformation prediction models and SBAS-InSAR in HR (reference date: March 28, 2017).

V. DISCUSSIONS

A. Spatio-temporal Characteristics for predicted Subsidence

The deformation caused by water-solution is significant in terms of spatial variation: from the Fig. 7 and Fig. 8 we can see the subsidence sequences shows significant subsiding characteristics for both the two test areas. For XH, each settlement funnel was gradually diffusing from the center to the surrounding area, which perfectly illustrates the substance diffusion and mass transfer law during the dissolution of salt substances. In order to show the boundary variations of each sub-settlement funnel more clearly, the boundaries of the settlement funnels are shown in Fig. 16. The accumulated areas of each sub-settlement funnel gradually increased temporally.
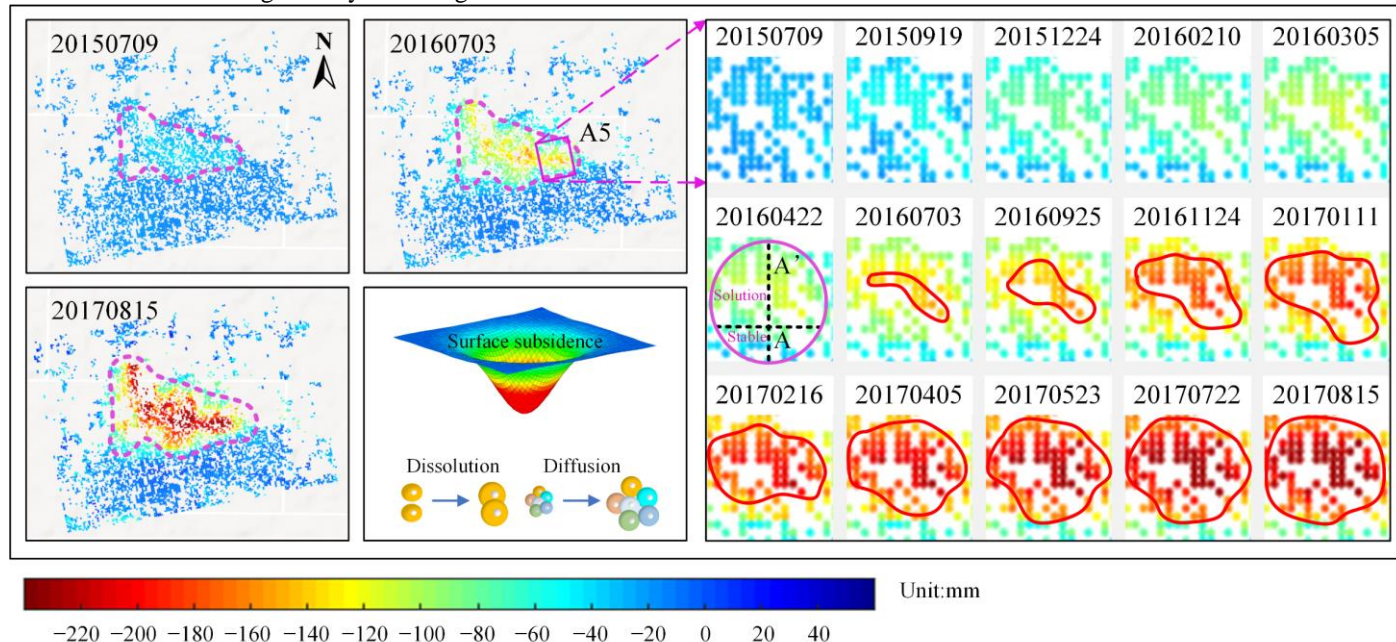

Fig. 16. Dynamical changes of the sub-settlement funnels in XR (reference date: June 15, 2015).

In order to clearly show the dissolution-diffusion characteristics, the deformation results of the extracted A5 settlement funnel were enlarged and shown as Fig. 16. The boundaries of the settlement funnel with subsidence greater than 120 mm are highlighted with red lines. By calculating the area of the pixel points, the settlement area greater than 120 mm was accumulated up to 664.7 m^2 on July 3, 2016, and increased to 5982.3 m^2 on August 15, 2017. The six sub-funnels are not separately distributed. Each funnel is with dark red in the center and progressively lighter from the center outwards. The funnels were becoming interconnected temporally during the spans. AA' profile in the April 22, 2016 image in Fig.16 was extracted for a profile analysis and shown as Fig. 17. As it shows, along AA' two kinds of subsidence can be derived spatially, stable area (from the starting to the 8th pixel) and solution area (from the 9th to the 30th pixel). Besides, it can also be found that the settlement funnel has multiple peaks of subsidence, respectively, with the maximum subsidence of 256 mm, 204 mm, and 109 mm, respectively. The multi-peak phenomenon is suggested related to the multi drilling wells distributed in A5.
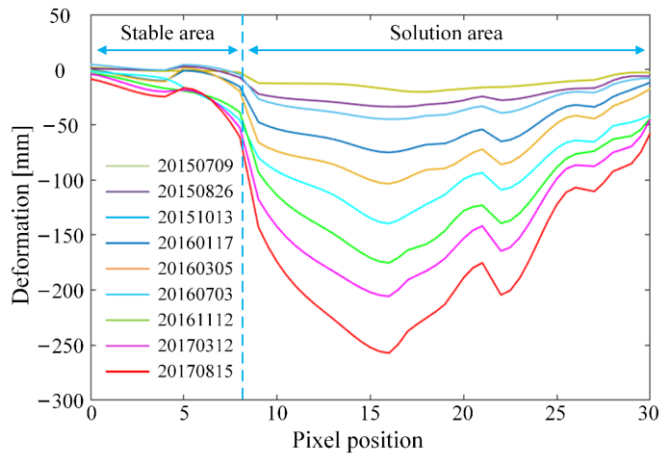

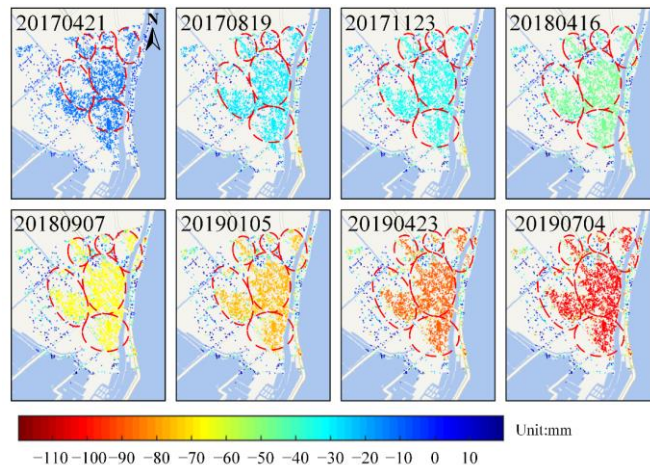**Fig. 17.** Profile analysis based on WSK deformation in XR.

Fig. 18. Dynamical changes of the sub-settlement funnels in HR (reference date: March 28, 2017).

Comparatively, the dissolution characteristics are not obvious for HR as shown in Fig. 18. Through the existed geological research [34], the salt mines located in HR have more than 40 years' mining history [35]. The super long-term mining activities caused the settlement funnels interconnected, with the salt material mainly dissolved along the vertical direction and horizontal dissolution rate close to zero. Consequently, a tendency of overall land subsiding characteristic dominated in HR.

To further analyze the temporal characteristics of the deformation results, five feature points were extracted in XR (F1-F5, as shown in Fig. 7) and HR (G1-G5, as shown in Fig. 8), respectively (as shown in Fig. 19 and Fig. 20). For the two groups, similar temporal evolution trend: total subsiding with seasonal fluctuations can be found from Fig. 19 and Fig. 20. The maximum subsidence was determined at F5 in XR and G5 in HR, respectively, with a maximum value of 296 mm and 147 mm, respectively.
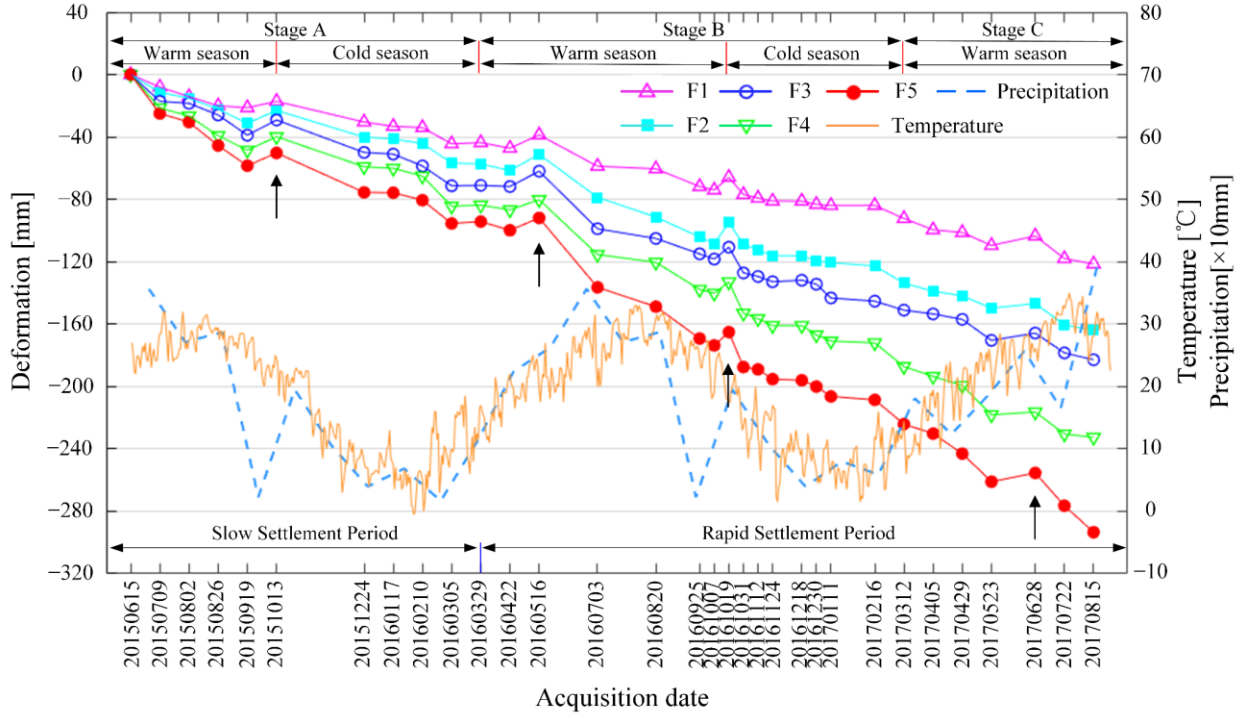

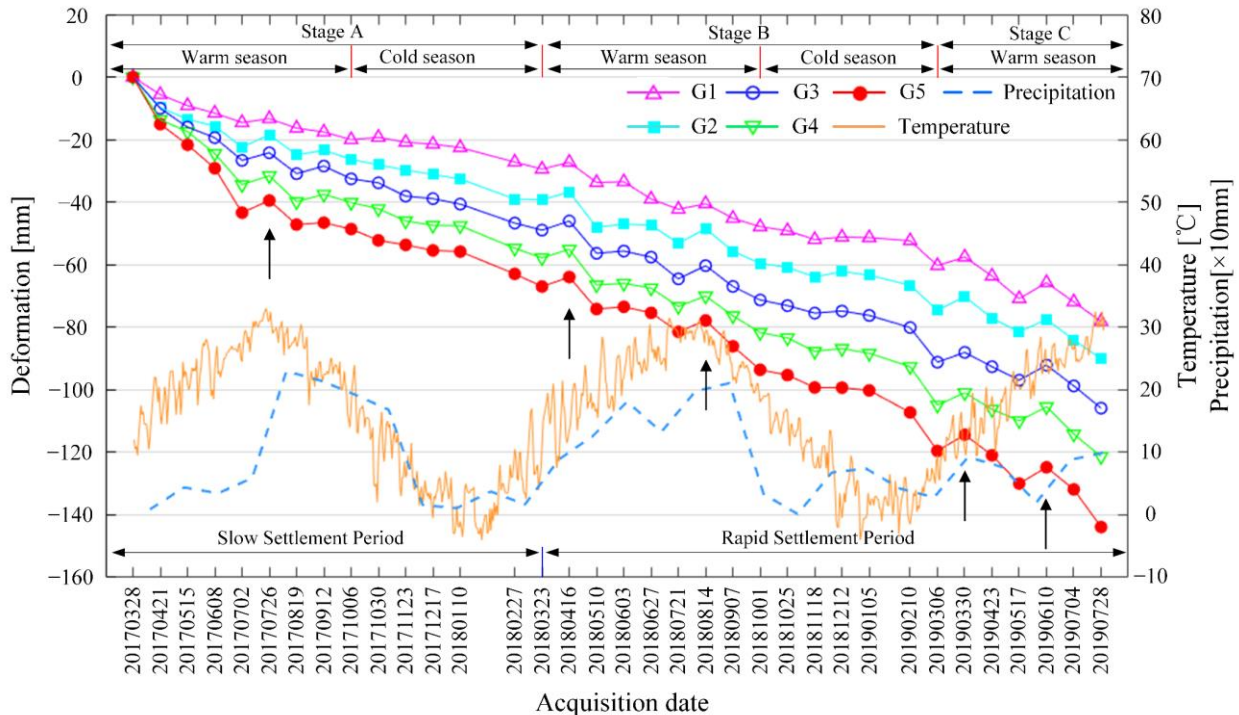**Fig. 19.** Time series settlement of feature points in XR (reference date: June 15, 2015).

Fig. 20. Time series settlement of feature points in HR (reference date: March 28, 2017).

TABLE IV
SOLUBILITY OF WATER-SOLUTION GLAUBER'S SALT AT DIFFERENT TEMPERATURES (G/100G H2O)

Mineral	Temperature (°C)										
	0	10	20	30	40	50	60	70	80	90	100
Thenardite	–	–	–	50.4	48.8	46.7	45.3	44.1	43.7	42.9	42.5
Glauber's salt	5.0	9.0	19.4	48.8	–	–	–	–	–	–	–
Glauberite	0.18	0.19	0.20	0.21	0.21	–	0.21	0.20	0.20	–	0.16

An interesting phenomenon of temporal seasonal variation has been revealed by our results. As shown in Fig 19 and Fig 20, rapid subsidence trends occurred at all the five feature points during the warm seasons (15 June 2015 to 13 October 2015 in Stage A, 29 March 2016 to 19 October 2016 in Stage B and March 12, 2017 to August 15, 2017 in Stage C for XR) and (28 March 2017 to 6 October 2017 in Stage A, 23 March 2018 to 1 October 2018 in Stage B, and March 6, 2019 to July 28, 2019 in Stage C for HR). In contrast, during the cold season in XR (October 13, 2015 to March 29, 2016 in Stage A, October 19, 2016 to March 12, 2017 in Stage B) and HR (October 6, 2017 to March 23, 2018 in Stage A, and October 1, 2018 to March 6, 2019 in Stage B), a relatively slow developing trend dominated these points. The main reason for this seasonal variation is that the dissolution rate of Glauber's salt is directly affected by the solvent temperature (as shown in Table IV) [41]. In the summer, the high temperature increases the solubility of the solvent, which accelerates the dissolution of Glauber's salt. On the contrary, in winter, the temperature of the solvent decreases due to the decrease in external temperature, which inhibits the dissolution of the Glauber's salt.

Another interesting phenomenon we discovered is that both XR and HR showed small jumps at the same time periods (marked black arrows in Fig. 19 and Fig. 20). This was not only related to the decrease in solubility caused by the above alternating winter and summer temperature, but also to the increase in precipitation [2], [42]. According to the collected precipitation and temperature data, the precipitation increased for both the four periods in both the two areas (as the four black narrows shown in Fig.19 and Fig.20. The recharge of external precipitation has exacerbated the uplift of surface deformation in the mining areas during those periods.

B. Sensitivity Analysis for WSK Parameters

It is important to analyze the sensitivity of the WSK parameters in order to understand how they affect the deformations and quantitative brine compositions. Suppose $SeS(D)$ and $SeS(C_x)$ as the sensitivity indices of the parameters D and C_x to the subsidence S_{sol}; $SeT(D)$ and $SeT(C_x)$ to the brine composition T_y, respectively. The Sobol index sensitivity analysis was adopted here.

Sobol indices are important sensitivity evaluation indices, which describe the global sensitivity of each parameter to the objective functions [43]. Firstly, the first-order indices K_α and total-effect indices K_α^{Tot} of the WSK parameters are calculated using variance analysis. Here K_α is the partial

variance, indicating the main contribution of a sample of the certain parameter to the output variances, where α is the certain parameter. K_α^{Tot} is the total variance, which describes the percentage of a group of samples for a certain parameter on the output variances; The perturbation analysis is then performed to quantitatively analyze the influences of each WSK parameter on the corresponding predicted deformations and brine compositions. The estimated indices for the two WSK parameters D and C_x are shown in Fig. 21, with the ranges of different levels of importance listed in Table V [43]. Fig. 21 shows that all the parameters are beyond the "Not correlated" range, which means they all have impacts on the accuracy of both the deformations and brine compositions, which cannot be ignored. It can be indicated that C_x is more sensitive than D in the model, with both values of K_α and K_α^{Tot} located in the range of [0.8, 1], accordingly treated as "Very important" parameter. This indicates that C_x shows high sensitivity on both the predicted subsidence and the extracted brine. A minor disturbance for C_x may cause significant errors on the predicted results. Comparatively, D shows relatively less sensitivity, with both values of K_α and K_α^{Tot} located within the range of "Important", except for K_α of the predicted deformations estimated as 0.48. Although it locates within the range of "un important", but still very close to the upper limit "0.5". Consequently, both the two WSK parameters we introduced into the InSAR model are highly sensitive and important, and accurate estimation is crucial for the forward prediction for both the deformations and the quantitative brine in salt mining area.
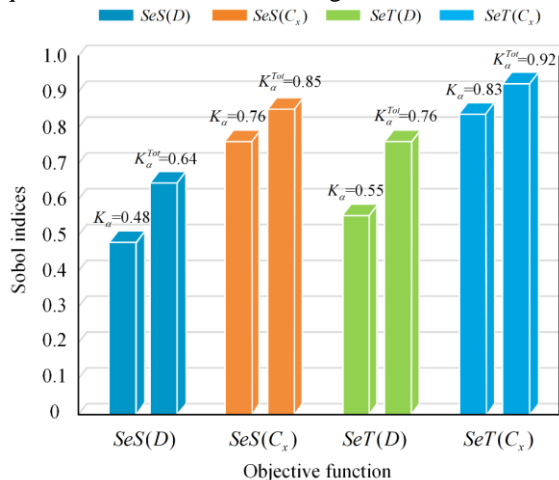

Fig. 21. Sensitivity analysis results of WSK parameters.

TABLE V
CORRELATION OF DIFFERENT SENSITIVITY INDICES RANGES.

Ranges of Sensitivity Indices	Correlation Extent
$0.8 < K_\alpha < K_\alpha^{Tot} \leq 1$	Very important
$0.5 < K_\alpha < K_\alpha^{Tot} \leq 0.8$	Important
$0.3 < K_\alpha < K_\alpha^{Tot} \leq 0.5$	Unimportant
$0 < K_\alpha < K_\alpha^{Tot} \leq 0.3$	Not correlated

VI. CONCLUSIONS

A novel InSAR deformation model based on Water-Solution Kinetic, namely WSK, was proposed and successfully applied in the forward prediction for both the time series deformations and quantitative extracted brine composition. It considers the principles of substance diffusion and mass transfer of salt, thus can be used directly for the quantitative prediction of both the deformations and extracted brine. Least Squares with Inequality Constraints (LSIC) is introduced to solve the unknown WSK parameters. Both simulated and real-data experiments were carried out to test the feasibility and reliability of the proposed method. The simulation showed that the RMSE between the predicted and the real subsidence was estimated as ±5.4 mm. In the real-data experiments, the maximum predicted deformation of the XR area and the HR area was 296 mm and 155 mm, respectively. The external accuracy for the deformation prediction was estimated as ±11.3 mm and ±7.2 mm, respectively. The comparative experiments with the traditional SBAS-InSAR and the Static-PIM algorithm showed that the accuracy of the WSK-predicted deformations was improved by 48.3% in XR and 54.5% in HR, respectively.

It can be concluded that the new approach has the following advantages: (1) WSK can reasonably reveal the non-linear characteristics of the time series deformations induced by water-soluble extraction in the salt mining areas: Spatially, with the single funnel but not separately distributed subsiding funnels around each water-soluble well, and with dark red in the center and progressively lighter from the center outwards. While temporally, the funnels were becoming interconnected during the spans and accompanied by significant seasonal fluctuations; (2) The WSK parameters can be directly estimated based on the InSAR phase observations, which can avoid the secondary error propagation of traditional PIM from InSAR inaccurate deformation observations to the subsequent predicted results; (3) LSIC algorithm, based on least squares estimation and with additional inequality constraints to ensure the uniqueness and stability, can avoid the time-consuming searching process of GA and significantly improve the accuracy and efficiency of parameter estimation; (4) WSK can be directly applied to the prediction of both the deformations and extracted brine composition, which provides a practical and reliable Remote Sensing method for quantitative brine quantity extraction estimation, and broadens the application of the InSAR technology.

REFERENCES

[1] Y. Cao, G. Y. Qiu, and Z. D. Zou, "Analysis on salt mine resources and its industrial situation in China," *Norg. Chem. Indus.*, vol. 50, no. 3, pp. 1–5, Mar. 2018.

[2] G. Y. Wang, P. Li, Z. H. Li, C. R. Liang, and H. J. Wang, "Coastal subsidence detection and characterization caused by brine mining over the Yellow River Delta using time series InSAR and PCA," *Int. J Appl. Earth Obs. Geoinf.*, vol. 114, pp. 103077. Nov.2022.

[3] V. Buchignani, G. D. Avanzi, R. Giannecchini, and A. Puccinelli, "Evaporite karst and sinkholes: a synthesis on the case of Camaiore (Italy)," *Environ. Geol.*, vol. 53, no. 5, pp. 1037–1044, May 2007.

[4] W. Y. Liu, F. Q. Han, J. L. Han, X. M. Yang, X. Q. Nian, and Q. F. Mao, "The application of gravity 3D focusing inversion in the brine exploration in dayantan area," *J. Salt Lake Res.*, vol. 26, no. 3, pp. 52–58, Sep. 2018.

[5] X. Y. Zhang, M. A. Hai-Zhou, D. L. Gao, X. U. Jian-Xin, and L. U. Juan-Chang, "Analysis of influencing factors causing the changes of chemical composition of underground brine in mining area of west Taijinar Salt Lake," *J. Salt. Lake. Res.*, vol. 17, no. 4, pp. 22–26, Dec. 2009.

[6] X. C. Yu, C. L. Wang, H. Huang, and J. Y. Wang, "Origin and evolution of Deep-seated K-rich brines in the paleogene of Qianjiang depression, Hubei Province," *Earth Scie.*, vol. 47, no. 1, pp. 122–135, Dec. 2009.

[7] J. C. Mura, F. F. Gama, W. R. Paradella, P. Negrão, S. Carneiro, C. G. Oliveira, and W. S. Brandão, "Monitoring the vulnerability of the dam and dikes in Germane iron mining area after the collapse of the tailings dam of Fundão (Mariana-MG, Brazil) using DInSAR techniques with TerraSAR-X data," *Remote Sens.*, vol. 10, pp. 1507, Sep. 2018.

[8] G. M. Zhang, Z. S. Wang, L. J. Wang, Y. L. Chen, Y. Wu, D. Ma, and K. Zhang, "Mechanism of collapse sinkholes induced by solution mining of salt formations and measures for prediction and prevention," *Bull. Eng. Geol. Environ.*, vol. 78, pp. 1401-1415, Nov. 2019.

[9] L. Xiao, Y. G. He, X. M. Xing, D. B. Wen, C. G. Tong, L. F. Chen, and X. Y. Yu, "Time series subsidence analysis of drilling solution miningrock salt mines based on Sentinel-1 data and SBAS-InSAR technique," *Nation. Remote Sens. Bulle.*, vol. 23, no. 3, pp. 501–513, Oct. 2019.

[10] S. L. Furst, S. Doucet, P. Vernant, C. Champollion, and J. L. Carme, "Monitoring surface deformation of deep salt mining in vauvert (France), combining InSAR and levelling data for multi-source inversion," *Solid Earth*, vol. 12, pp. 15–34, Jan. 2021.

[11] F. F. Gama, A. Cantone, J. C. Mura, P. Pasquali, W. R. Paradella, A. R. dos Santos, and G. G. Silva, "Monitoring subsidence of open pit iron mines at Carajás Province based on SBAS interferometric technique using TerraSAR-X data," *Remote Sens. Appl.*, vol. 8, pp. 199–211, Sep. 2017.

[12] M. N. Zheng, K. Z. Deng, H. D. Fan, and S. Du, "Monitoring and analysis of surface deformation in mining area based on InSAR and GRACE," *Remote Sens.*, vol. 10, pp. 1392, Sep. 2018.

[13] Y. Chen, Y. X. Tong, and K. Tan, "Coal mining deformation monitoring using SBAS-InSAR and offset tracking: A case study of Yu County, China," *IEEE J. Sel. Top. Appl. Earth Obs. Remote Sens.*, vol. 13, pp. 6077-6087, Oct. 2020.

[14] T. Ma, Y. J. Zhao, and W. Zhang, "Application of SBAS-InSAR technology in settlement monitoring of mining area," *Geom. Spat. Inf. Tech.*, vol. 43, no. 11, pp. 210–212, Nov. 2020.

[15] Z. F. Yang, Z. W. Li, J. J. Zhu, J. Hu, Y. J. Wang, and G. L. Chen, "InSAR-Based model parameter extraction of probability integral method and its application for predicting mining-induced horizontal and vertical displacements," *IEEE Trans. Geosci. Remote Sens.*, vol. 54, no. 8, pp. 4818–4832, Apr. 2016.

[16] H. F. Fan, L. Lu, and Y. H. Yao, "Method combining probability integration model and a small baseline subset for time series monitoring of mining subsidence," *Remote Sens.*, vol. 10, pp. 1444, Sep. 2018.

[17] J. J. Zhu, Z. F. Yang, Z. W. Li, and J. Hu, "A mining monitoring method based on InSAR technology," Chinese patents ZL201310011306.2, May 8, 2013.

[18] Z. F. Yang, Z. W. Li, J. J. Zhu, A. Preusse, H. W. Yi, Y. J. Wang, and M. Papst, "An extension of the InSAR-Based probability integral method and its application for predicting 3-D Mining-induced displacements under different extraction conditions," *IEEE Trans. Geosci. Remote. Sens.*, vol. 55, no. 7, pp. 3835–3845, Mar. 2017.

[19] Z. F. Yang, Z. W. Li, J. J. Zhu, G. C. Feng, Q. J. Wang, J. Hu, and C. C. Wang, "Deriving time series three-dimensional displacements of mining areas from a single-geometry InSAR dataset," *J. Geod.*, vol. 92, no. 5, pp. 529–544, Sep. 2018.

[20] X. M. Xing, Y. K. Zhu, Z. H. Yuan, L. Xiao, X. B. Liu, L. F. Chen, Q. Xia, and B. Liu, "Predicting mining-induced dynamic deformations for drilling solution rock salt mine based on probability integral method and weibull temporal function," *Int. J. Remote Sens.*, vol. 42, no. 2, pp. 639–671, Nov. 2020.

[21] Z. F. Yang, Z. W. Li, J. J. Zhu, H. W. Yi, J. Hu, and G. C. Feng, "Deriving dynamic subsidence of coal mining areas using InSAR and logistic model," *Remote Sens.*, vol.9, no.2, pp.125, Feb.2017.

[22] L. J. Zhu, X. M. Xing, Y. K. Zhu, Z. H. Yuan, and Q. Xia, "An advanced time series InSAR approach based on poisson curve for soft clay expressway deformation monitoring," *IEEE J. Sel. Top. Appl. Earth Obs.*, vol.14, pp.1–16, Jul.2021.

[23] Q. M. Wang, "Drilling water solution mining and design," China, Beijing: *Chem. Ind. Press*, Nov. 2016, pp. 59-63.

[24] P. Berardino, G. Fornaro, R. Lanari, and E. Sansosti, "A new algorithm for surface deformation monitoring based on small baseline differential SAR interferograms," *IEEE Trans. Geosci. Remote. Sens.*, vol. 40, no. 11, pp. 2375–2383, Nov, 2002.

[25] D. Li, K. Z. Deng, X. X. Gao, and H. P. Niu, "Monitoring and analysis of surface subsidence in mining areas based on SBAS-InSAR," *Geom. Inf. Sci. Wuhan Univ.*, vol. 43, no. 10, pp. 1531–1537, 2018.

[26] T. R. Lauknes, H. A. Zebker, and Y. Larsen, "InSAR deformation time series using an l1-norm small-baseline approach," *IEEE Trans. Geosci. Remote Sens.*, vol. 49, no. 1, pp. 536–546, Jul. 2010.

[27] Y. Zhang, X. M. Meng, C. Jordan, A. Novellino, T. Dijkstra, G. Chen, "Investigating slow-moving landslides in the Zhouqu region of China using InSAR time series," *Landslides*, vol. 5, no. 7, pp. 1–17, Jan. 2018.

[28] J. J. Zhu, and J. Xie, "A simple iterative algorithm for inequality constrained adjustment," *Acta. Geo. Cartogr. Sin*, vol. 40, no. 2, pp. 209–212, Apr. 2011.

[29] Y. H. Peng, and D. J. YU, "Comparison of least squares methods with inequality constraints," *Beijing Surve. Map.*, vol. 33, no. 12, pp. 1470–1473, Dec. 2019.

[30] X. M. Xing, H. C. Chang, L. F. Chen, J. H. Zhang, Z. H. Yuan, and Z. N. Shi, "Radar interferometry time series to investigate deformation of soft clay subgrade settlement—A case study of Lungui Highway, China," *Remote Sens.*, vol. 11, no. 4, pp. 429, Feb. 2019.

[31] Y. K. Zhu, X. M. Xing, L. Bao, and L. F. Chen, "Surface deformation retrieving over soft clay based on an improved time series InSAR model: a case study of Dongting lake area, china," *IEEE Access*, vol. 8, pp. 195703–195720, Oct. 2020.

[32] X. M. Xing, Y. K. Zhu, W. B. Xu, W. Peng, and Z. H. Yuan, "Measuring subsidence over soft clay highways using a novel time series insar deformation model with an emphasis on rheological properties and environmental factors (NREM)," *IEEE Trans. Geosci. Remote. Sens.*, vol. 60, pp. 1–19, Feb. 2022.

[33] X. M. Xing, T. F. Zhang, L. F. Chen, Z. F. Yang, X. B. Liu, W. Peng, and Z. H. Yuan, "InSAR modelling and deformation prediction for salt solution mining using a novel CT-PIM function," *Remote. Sens.*, vol. 14, pp. 842, Feb. 2022.

[34] P. Zhu, Z. C. Liu, and Y. Zheng, "Analysis on structural configurations and influence factors of the dissolved salt cavity with solution mining in Huaian," *China Wel. Roc. Sal.*, vol. 51, no. 5, pp. 6–9, Sep. 2020.

[35] X. M. Li, Q. Q. Jiang, W. Q. Zhu, Z. C. Liu, and J. F. Wu, "Analysis on the ledge comparison and the distribution characteristics of the salt mine on the Zhaoji mining area, Hongze Sag," *China Wel. Roc. Sal.*, vol. 49, no. 5, pp. 16–19, Sep. 2018.

[36] R. M. Goldstein, and C. L. Werner. "Radar interferogram filtering for geophysical applications," *Geophys. Res. Lett.*, vol. 25, no. 21, pp. 4035–4038, Nov. 1998.

[37] Z. W. Li, X. L. Ding, D. W. Zheng, and C. Huang, "Least squares-based filter for remote sensing image noise reduction," *IEEE Trans. Geosci. Remote Sens.*, vol. 46, no. 7, pp. 2044–2049, Jul. 2008.

[38] W. Peng, Q. J. Wang, F. B. Zhan, and Y. M. Cao. "Spatiotemporal Ocean Tidal Loading in InSAR measurements Determined by Kinematic PPP Solutions of a Regional GPS Network," *IEEE J. Sel. Top. Appl. Earth Obs. Remote Sens.*, vol. 13, pp. 3772–3779, Jun. 2020.

[39] R. Zhao, Z. W. Li, G. C. Feng, Q. J. Wang, and J. Hu, "Monitoring surface deformation over permafrost with an improved SBAS-InSAR algorithm: With emphasis on climatic factors modelling," *Remote Sens. Environ.*, vol. 184, pp. 276–287, Oct. 2016.

[40] H. D. Fan, D. Cheng, K. Z. Deng. B. Q. Chen, and C. G. Zhu, "Subsidence monitoring using D-InSAR and probability integral prediction modelling in deep mining areas," *Surv. Rev.*, vol. 47, no. 345, pp. 438–445, Jan. 2015.

[41] Z. Y. Ma, C. X. Nie, and R. T. Wang. "Geological basis and mining technology of well and mineral salt," China, *Nat. Mine salt inf.*, pp.82–115, Oct. 1992.

[42] M. Fomelis, E. Papageorgiou, and C. Stamatopoulos, "Episodic ground deformation signals in Thessaly Plain (Greece) revealed by data mining of SAR interferometry time series," *Int. J. Remote Sens.*, vol. 37, no. 16, pp. 3696–3711. Dec. 2016.

[43] F. Cannavo, "Sensitivity analysis for volcanic source modelling quality assessment and model selection," *Comput Geosci-UK.*, vol. 44, pp. 52–59, Mar. 2012.

Xuemin Xing (Member, IEEE) was born in Liaoning, China, in 1983. She received the B.S. and M.S. degrees and the Ph.D. degree in geomatics and surveying from Central South University, Changsha, China, in 2005, 2008, and 2011, respectively. From 2016 to 2017, she was a Visiting Scholar with the Department of Environmental Sciences, Macquarie University, Sydney, NSW, Australia. She is currently a Professor with the School of Traffic and Transportation Engineering, Changsha University of Science and Technology, Changsha, where she is also a Key Member of the Institute of Radar Remote Sensing Applications for Traffic Surveying and Mapping. She is also a reviewer for more than ten international journals and national journals in China. She has authored more than 70 articles and 10 inventions.

Her research interests include the application of time-series interferometric synthetic aperture radar (InSAR) technique in traffic infrastructures deformation monitoring, deriving spatial–temporal large-scale deformation induced by mining activities and modelling.

Tengfei Zhang (Student Member, IEEE) was born in Henan, China, in 1995. He received the B.S. degree in geomatics and surveying from the Zhengzhou Technology and Business University, Zhengzhou, China, in 2020 and the M.S. degree in surveying and mapping science and technology from the Changsha University of Science and Technology, Changsha, China, in 2023. He is currently pursuing his Ph.D. degree at the School of Resource and Environment Science, Wuhan University, Wuhan, China.

His research interests include the application of MT-InSAR technology for deformation monitoring in salt solution mining.

Jun Zhu was born in Hunan, China, in 1986. he received the B.S. degree in Changsha University of Science and Technology in 2008, and received the B.S. and M.S. degrees and the Ph.D. degree in geomatics and surveying from Central South University, Changsha, China, in 2011, and 2017, respectively. He is currently a Lecturer at Changsha University of Science and Technology, Changsha, China.

His main research areas included high-resolution interferometric data processing based on instantaneous frequency estimation and the study of desert penetration depth and physical property inversion using PolInSAR technology. He has authored more than 10 papers in domestic and international academic journals, including 8 papers as the first or corresponding author, and 6 papers in SCI/EI journals.

Jiancun Shi was born in Henan, China. She received the B.E. degree in geomatics from Qinghai University, Xining, China, in 2015, the M.S. degree in surveying science and technology from China University of Geosciences, Beijing, China, in 2018, and the PhD degree in surveying science and technology from Central South University, Changsha, China, in 2022. She is currently a Lecturer at Changsha University of Science and Technology, Changsha, China.

Her research interests are deformation monitoring and modelling of surface facilities in mining areas by InSAR technology.

Jiehua Cai was born in Hunan, China, in 1992. He received the B.S. degree in Geo-information Science and Technology from Ocean University of China, Qingdao, China, in 2015, the M.S. degree in surveying and mapping engineering from Central South University, Changsha, China, in 2018, and received the PhD degree in photogrammetry and remote sensing from Wuhan University, Wuhan, China, in 2022. He is currently a Lecturer at Changsha University of Science and Technology, Changsha, China.

His research interests include synthetic aperture radar (SAR), deformation monitoring, deep learning, geological disaster detection and monitoring.

Guanfeng Zheng was born in Guangdong, China, in 1998. He received the B.S. degree in geomatics and surveying from the Changsha University of Science & Technology, Hunan, China, in 2021. He is currently pursuing his M.S. degree in Civil and Hydraulic Engineering, Changsha University of Science and Technology, Hunan, China.

His research interests include the application of time series InSAR technique for deformation estimation of soft clay area.

Minchao Lei was born in Hunan, China, in 1998. He received the B.S. degree in Geographic Information Science from the Hunan University of Arts and Science, Hunan, China, in 2021. He is currently pursuing his M.S. degree in surveying and mapping science and technology at the Changsha University of Science and Technology, Changsha, China.

His research interest in application of MT-InSAR technique for Three-dimensional deformation of the mining area.